IEEE Access
Multidisciplinary ⋮ Rapid Review ⋮ Open Access Journal

Received 26 January 2026, accepted 23 February 2026, date of publication 2 March 2026, date of current version 5 March 2026.

Digital Object Identifier 10.1109/ACCESS.2026.3669499

RESEARCH ARTICLE

Graph-Transformer for Spatiotemporal Soil Moisture Forecasting Using Multimodal Remote Sensing Data

MAHDI SAKI, DANIEL FRANKLIN, (Member, IEEE), MEHRAN ABOLHASAN, (Senior Member, IEEE), JUSTIN LIPMAN, (Senior Member, IEEE), AND NEGIN SHARIATI, (Senior Member, IEEE)

RF and Communication Technologies (RFCT) Research Laboratory, School of Electrical and Data Engineering, Faculty of Engineering and IT, University of Technology Sydney, Ultimo, NSW 2007, Australia

Corresponding author: Mahdi Saki (Mahdi.Saki@uts.edu.au)

This work was supported in part by NTT Group and the Food Agility Cooperative Research Centre (CRC) Ltd., funded by the Commonwealth Government CRC Program for the "Sustainable Sensing, Enhanced Connectivity, and Data Analytics for Precision Urban and Rural Agriculture" Project with the RF and Communication Technologies (RFCT) Research Laboratory, University of Technology Sydney (UTS).

ABSTRACT Soil moisture is a key variable in the hydrological cycle, essential for drought monitoring, water resource management, and agriculture decision-making. However, accurate forecasting of soil moisture remains a challenge due to the nonlinear nature of soil water dynamics and the complex influencing factors. While deep learning models such as Long Short-Term Memory and Transformers have advanced temporal modelling, they struggle with spatial dependencies across diverse geographic locations, as their architecture primarily focuses on temporal dynamics. To address this limitation, we propose a novel hybrid framework that integrates graph neural networks with state-of-the-art time series models. We introduce a Graph-Transformer architecture for improved soil moisture forecasting by jointly modelling spatiotemporal dependencies. Our model forecasts soil moisture at two depths including 0–7 cm, referred to as surface soil moisture (SSM), and 7–28 cm, representing the root-zone soil moisture (RZSM). Evaluation using four years of multimodal data from 19 sites across Australia shows that the proposed Graph-Transformer model outperforms the standard Transformer, achieving improvements of up to 10% in the coefficient of determination (R^2) and 8% in Root Mean Square Error (RMSE) for SSM, and up to 11% and 9% in R^2 and RMSE, respectively, for RZSM. These findings highlight that integrating graph architecture with temporal models can potentially enhance soil moisture forecasting across diverse geographic regions, benefiting effective drought monitoring and agricultural planning.

INDEX TERMS Deep learning, graph neural networks, graph transformers, remote sensing, root-zone soil moisture, soil moisture forecasting, spatiotemporal modeling, surface soil moisture.

I. INTRODUCTION

Soil moisture (SM) plays a vital role in the Earth's hydrological, energy, and carbon cycles, with significant implications for drought monitoring, water resource management, irrigation scheduling, and climate modelling [1]. Accurate forecasting of SM is essential for anticipating agricultural productivity, managing hydrological extremes, and optimizing environmental decision-making [2]. However, predicting SM is inherently challenging due to its high spatiotemporal variability and dependence on a complex interplay of meteorological, land surface, and root-zone processes [3]. Traditionally, SM forecasting has relied on three primary approaches: physics-based land surface models, in-situ sensor networks, and satellite-based remote sensing (RS) techniques [4]. Physics-based models such as

The associate editor coordinating the review of this manuscript and approving it for publication was Xin Sun.

© 2026 The Authors. This work is licensed under a Creative Commons Attribution 4.0 License.
For more information, see https://creativecommons.org/licenses/by/4.0/

NOAH and VIC [5] simulate SM distributions using water balance equations constrained by meteorological forcing and land surface parameters. While these models offer physically interpretable outputs, they often suffer from high parameter sensitivity, scale mismatch, and uncertainties in forcing data and soil characteristics leading to reduced accuracy in regions with sparse ground observations or highly heterogeneous landscapes [6]. In-situ measurements [7], [8], [9], though accurate at point scale, are spatially limited and logistically challenging to maintain at large scales, making them insufficient for regional to global applications [10]. To address these limitations, RS-based SM products derived from passive and active microwave sensors such as Soil Moisture Active Passive (SMAP), Advanced Microwave Scanning Radiometer for EOS (AMSR-E) and Sentinel-1 have become increasingly popular due to their broad spatial coverage and regular acquisition [11]. Nevertheless, individual RS products often exhibit trade-offs between spatial resolution, revisit frequency, and retrieval accuracy under varying surface and vegetation conditions [12]. Furthermore, satellite observations are frequently affected by retrieval gaps due to radio frequency interference, dense vegetation, frozen soil, or sensor limitations, which hinder their direct use in continuous forecasting applications [13]. Recent efforts have explored data fusion approaches to combine multiple RS products, leveraging their complementary strengths to produce more complete and reliable SM datasets. Strategies such as spatiotemporal interpolation [14], weighted averaging [15], and machine learning (ML) based fusion [16] have shown promise in improving the quality of SM inputs for forecasting. However, selecting optimal combinations of RS products, aligning them temporally and spatially, and mitigating inconsistencies remain open challenges, especially in operational settings [17]. ML techniques have emerged as powerful tools for SM forecasting due to their ability to learn nonlinear relationships from large and heterogeneous data sources [18], [19], [20], [21]. For timeseries forecasting, recurrent neural networks (RNNs) and attention-based models are the state-of-the-art methods [22], [23]. RNNs, particularly Long Short-Term Memory (LSTM) networks, have been widely adopted for their sequence modelling capabilities, while attention-based models such as Transformers have demonstrated superior performance in capturing long-range temporal dependencies [24]. These models have been successfully applied to forecast surface and root-zone SM using time series of RS inputs and meteorological variables [25], [26], [27], [28]. Despite their strengths, time series-based ML models for SM forecasting are inherently more effective at capturing temporal patterns but often struggle to model spatial dependencies [28]. A common workaround is to train separate models for each location, treating sites independently [27]. However, this independence assumption limits the generalization of the model and can result in suboptimal performance, particularly in data-sparse regions where site-specific training data are insufficient [29]. Incorporating spatial context is essential to exploit spatial autocorrelation and shared dynamics across neighbouring regions, thereby enhancing model robustness and improving forecast accuracy [30]. Graph-based learning frameworks, particularly Graph Neural Networks (GNNs), offer a natural and flexible approach for modelling spatial dependencies among geographically distributed sites [31]. By encoding spatial proximity, environmental similarity, or other domain-specific relationships within a graph structure, GNNs facilitate information sharing across locations during model training. When integrated with temporal models such as Transformers, this combination provides a powerful framework for capturing both spatial and temporal dependencies, resulting in more accurate and spatially coherent SM forecasts. Graph-Transformer architectures have been successfully applied in a range of domains, including molecular property prediction [32], traffic flow forecasting [33], social network analysis [34], and recommender systems [35], where capturing both structural relationships and sequential patterns is essential. However, to the best of our knowledge, no prior work has investigated the use of Graph-Transformers for SM forecasting. Therefore, this study proposes a hybrid Graph-Transformer architecture that leverages multimodal RS and meteorological data to advance SM forecasting across multiple forecast horizons and at two soil depths, including both surface (0–7 cm) and root-zone (7–28 cm). The key contributions of this study are as follows:

- The introduction of a novel Graph-Transformer network for SM forecasting, leveraging the strengths of graph-based spatial modelling and Transformer-based temporal sequence learning to effectively capture complex spatiotemporal dependencies.
- Integration of multimodal remote sensing data from multiple satellite missions and products including SM, soil temperature, meteorological variables, vegetation indices, land surface temperature (LST), and radar backscatter to improve forecasting accuracy.
- Development of forecasting models for two distinct soil depths, 0–7 cm and 7–28 cm, allowing for a comprehensive assessment of both surface and root-zone moisture dynamics.
- Comprehensive evaluation of the proposed model using four years of data from 19 locations across Australia, demonstrating that the model consistently outperformed baseline models across multiple forecast horizons and diverse land cover types.

For clarity and consistency with ERA5 terminology, we refer to SSM and RZSM as layer 1 and layer 2, respectively, throughout this paper. These terms are used interchangeably, as summarized in Table 1.

TABLE 1. Mapping of soil moisture terms to layer definitions and depth ranges.

Term	Layer	Depth Range
Surface Soil Moisture	layer 1	0–7 cm
Root-Zone Soil Moisture	layer 2	7–28 cm

II. STUDY MATERIALS

A. STUDY AREA AND IN-SITU DATA

This study area spans the continent of Australia (both the mainland and Tasmania), with sensors located at 19 sites across different soil types, climate and land cover. Ground truth data is obtained from the Australian Cosmic-ray Neutron Soil Moisture Monitoring (CosmOz) Network [36]. Fig. 1 presents the spatial distribution of the in-situ SM monitoring stations used in this study across Australia. Additionally, Table 2 provides detailed site-level metadata for each monitoring station including geographic coordinates, land cover classifications, bulk density, and elevation.

The CosmOz network uses cosmic-ray probes (CRPs) along with time-domain reflectometry (TDR) sensors to measure SM as a volume percentage at different locations around Australia with hourly resolution since 2010. The data samples for each site are publicly available at https://cosmoz.csiro.au/sites For this study, we collated data from 2020-11-10 to 2024-12-10.

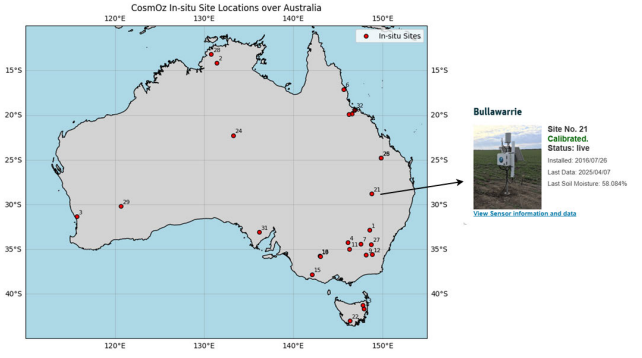

FIGURE 1. Study area showing the locations of in-situ soil moisture monitoring stations across australia.

The CosmOz network provides in-situ SM measurements at a variety of depths, typically ranging from approximately 5 cm to 60 cm, depending on soil wetness conditions. This depth variability can present challenges when validating satellite-based SM products at a surface level, necessitating filtering techniques to ensure comparability [36], [37], [38]. However, the variability in CosmOz measurements makes it a valuable reference for evaluating SM products across various satellites at multiple soil layers [39], [40]. Accordingly, we used CosmOz in-situ data to identify the most suitable satellite-based SM targets for training and evaluating our models at different depths. A detailed analysis is provided in Section II-C.

B. REMOTE SENSING DATA

The RS dataset collection employed in this study is notable for its comprehensiveness, offering a diverse suite of variables including vegetation indices, LST, elevation, land cover, meteorological parameters, soil properties, and SM. These variables support a broad spectrum of Earth observation applications such as SM modelling, land surface process analysis, vegetation monitoring, hydrological modelling, and climate studies. To ensure both relevance and continuity, we systematically reviewed the relevant studies published since 2019 that utilized satellite-based data for SM prediction. Based on this review, we compiled a broad inventory of RS products and shortlisted only those that are still operational, thereby excluding discontinued missions or failed satellite products. Table-S1 in the Supplementary Materials presents the selected RS datasets used in this study, detailing the associated variables, data products available through Google Earth Engine (GEE) [41], spatial and temporal resolutions, availability periods, and supporting references. These datasets form the foundation of our multimodal analysis and provide a benchmark resource for future research in SM prediction and related domains. The datasets in Table-S1 are grouped into several key categories that collectively capture the dynamics of land surface and atmospheric conditions relevant to SM estimation. These categories include vegetation indices, LST, surface reflectance, elevation, land cover, meteorological variables, soil properties, SM, and radar backscatter. Each category contains variables that are derived from specific satellite missions or RS products. The inclusion of these diverse data types allows for a comprehensive representation of the environmental and physical processes influencing SSM and RZSM dynamics. Soil properties are sourced from OpenLandMap [42], [43], encompassing variables such as soil texture, bulk density, sand/clay content, organic carbon, pH, and water content. These static datasets are typically provided at a spatial resolution of 250 meters, meaning that each data point represents the average soil property value within a 250 $\times$ 250 m^2 grid cell. This resolution offers sufficient spatial detail to support soil hydraulic modelling and enables the estimation of parameters such as plant available water capacity and retention characteristics [44], [45].

C. SATELLITE-BASED SM DATA

The SM category comprises several products from GLDAS and SMAP (L3 and L4) and ERA5. SMAP datasets provide global SM observations at daily to 3-hourly intervals and spatial resolutions between 9 and 11 km [46], [47]. GLDAS includes model-based estimates of RZSM and SSM at a coarser spatial resolution of 27 km [48]. The ERA5-Land dataset provides a high-resolution, multi-decadal reanalysis of land surface variables, generated by reprocessing the land component of the ECMWF ERA5 climate [49]. By assimilating global observations within a physically consistent modelling framework, ERA5-Land offers spatially and temporally coherent data spanning several decades, thereby facilitating detailed retrospective analyses of land surface processes. The dataset comprises a comprehensive suite of 50 variables and is publicly accessible via the Copernicus Climate Data Store [50]. ERA5 provides SM estimates across 4 vertical layers, including layer 1 (0–7

TABLE 2. Summary of site characteristics for the in-situ soil moisture monitoring stations used in this study. Missing site numbers correspond to stations that were decommissioned or inoperative during the study period.

Site no.	Site name	Latitude	Longitude	Land cover/use	Bulk density	Elevation
2	Daly	-14.15919	131.3881	Tropical savanna	1.458	75
3	Gnangara	-31.37669	115.7132	Woodland	1.328	50
6	RobsonCk	-17.11647	145.62958	Tropical rainforest	1.056	715
7	Temora	-34.4046	147.53255	Agricultural site	1.506	294
8	Tullochgorum	-41.66942	147.91167	Grazing land	1.248	285
10	WeanyCk	-19.88195	146.53599	Grazed open woodland with grassy and shrubby understory	1.655	287
11	Yanco	-35.00499	146.29917	Grazing land	1.532	124
15	Hamilton	-37.828	142.0895	Pasture grazed	1.078	199
18	Bishes	-35.76943	142.97258	Grazing/agricultural	1.489	94
19	Bennets	-35.8258	143.00415	Grazing land	1.37	98
21	Bullawarrie	-28.80932	148.76512	Agricultural site	0.957	166
23	BCS Conservatively Grazed (C3)	-24.81241	149.80126	Grazed buffel grass pasture	1.403	165
25	BCS Brigalow Woodland (C1)	-24.815392	149.794076	Woodland	1.248	175
26	BCS Heavily Grazed (C5)	-24.810658	149.790157	Grazed buffel grass pasture	1.493	168
24	AliceMulga	-22.28233	133.251135	Arid and semi-arid land	1.57	607
27	Boorowa	-34.47134	148.69688	Grazing land	1.457	165
29	Credo	-30.1913	120.65413	Temperate woodland	1.175	450
30	Fletcherview	-19.887062	146.189741	Open savanna woodland	1.709	260
32	OakValley	-19.438902	146.82694	Open grassy area	1.632	45

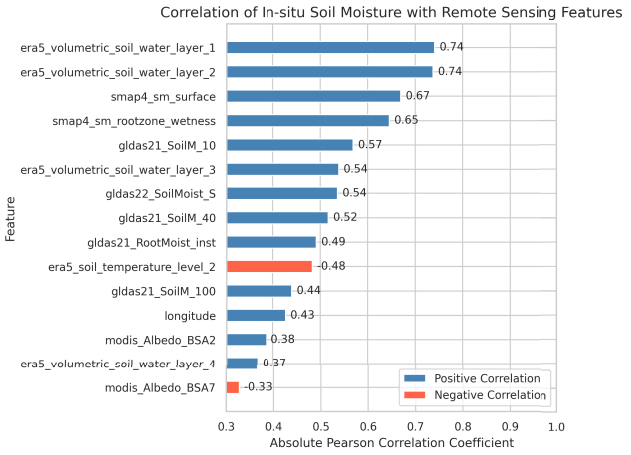

FIGURE 2. Absolute pearson correlation coefficients between in-situ soil moisture and remote sensing-based features with correlations greater than 0.3. Features with positive correlations are shown in blue, while those with negative correlations are shown in red.

cm), layer 2 (7–28 cm), Layer 3 (28–100 cm), and Layer 4 (100–289 cm). In this study, we utilize layers 1 and 2, which exhibit the highest correlation with the CosmOz in-situ measurements, to train and evaluate models for forecasting SSM and RZSM. Fig. 2 presents the correlations between the in-situ and satellite-based SM features, including those with correlation coefficients greater than 0.3. As illustrated, the volumetric soil water content from ERA5 layers 1 and 2 shows the highest correlation exceeding 0.7 with in-situ SM, outperforming all other features.

D. OTHER AUXILIARY DATA

Additional features used as auxiliary data include vegetation indices, LST, elevation, land cover information, meteorological variables, and Synthetic Aperture Radar (SAR) data from Sentinel-1. A summary of all auxiliary data utilized in this study is provided in Table-S1. The vegetation indices category includes products from both Moderate Resolution Imaging Spectroradiometer (MODIS) and Visible Infrared Imaging Radiometer Suite (VIIRS), providing enhanced vegetation index (EVI) and normalized difference vegetation index (NDVI) at spatial resolutions ranging from 500 m to 1 km and temporal resolutions from 16-daily to daily. These indices serve as proxies for vegetation health, density, and phenology, all of which modulate evapotranspiration and influence SM [51]. MODIS MYD13A2 and VIIRS VNP13A1 products are widely used in ecohydrological studies due to their continuity and consistency [52], [53]. The LST category includes multiple datasets from MODIS (e.g., MOD11A1, MOD11A2, MCD43A3), VIIRS (VNP21A1D and VNP21A1N), and Landsat 8 (LC08/C02/T1_L2). These datasets provide critical insights into surface energy balance and are essential for understanding evaporation and heat fluxes at various spatial and temporal scales [26], [44], [52], [53], [54], [55], [56]. Daily and 8-day LST observations are available at resolutions of 1 km (MODIS and VIIRS) and 30 m (Landsat), making them useful for both regional and site-specific studies. Additionally, the LST category includes surface albedo data [56] derived from the MODIS MCD43A3 product, which provides daily measurements at 500 m resolution. Albedo represents the fraction of incoming solar radiation reflected by the Earth's surface and plays a fundamental role in determining the surface energy balance. Its inclusion enhances the interpretation of LST by offering information about surface radiation dynamics, particularly in models estimating evapotranspiration and net radiation. Therefore, the albedo dataset complements LST measurements and broadens the analytical capacity of RS applications in hydrology, climate monitoring, and land surface process modeling [56]. The surface reflectance products, primarily from Terra MODIS including MOD09GA and MOD09A1, provide calibrated spectral reflectance values

that underpin the derivation of vegetation indices and land surface characterization. These datasets are available at 500 m resolution and daily or 8-day intervals and are crucial for land surface classification, change detection, and assimilation into biophysical models [25], [44], [56], [57]. The elevation category comprises digital elevation models (DEMs) from multiple sources including ALOS DSM, MERIT DEM, SRTM, and HydroSHEDS. These products offer various resolutions, from 30 m in ALOS to 93 m in MERIT and HydroSHEDS. Elevation and topographic attributes influence soil water movement, drainage patterns, and site wetness potential, making them vital for hydrological and terrain-based modelling [45], [53], [56], [58]. Land cover information is represented by the MODIS MCD12Q1 dataset, which provides annual global land cover classifications at 500 m resolution from 2001 to 2023. This dataset aids in distinguishing land use types and vegetation regimes, which directly impact infiltration, evapotranspiration, and surface runoff characteristics, thus influencing SM dynamics [56]. The meteorological variables include precipitation, air temperature, surface pressure, humidity, and wind speed, derived from CHIRPS, ERA5-Land, and GLDAS-2.1/2.2. These variables are key drivers of soil water balance and are available at various temporal resolutions including daily for ERA5-Land and CHIRPS, and 3-hourly for GLDAS products [44], [45], [55], [56]. Their spatial resolutions range from 5.6 km in CHIRPS to 27 km in GLDAS, providing flexibility for multi-scale hydrological modelling and data assimilation studies. The radar backscatter is represented by Sentinel-1 SAR data, which is available at a high spatial resolution of 10 m and revisit times ranging from 3 to 12 days depending on location. Although not a direct SM measurement, radar backscatter is sensitive to surface moisture, roughness, and vegetation cover, making it a valuable input for SAR-based SM retrieval models [44], [57], [59].

III. METHODS

A. OVERALL WORKFLOW

The overall workflow used in this study to forecast SM from multimodal RS and in-situ data is illustrated in Fig. 3. Four years of 3-hourly in-situ SM observations from 19 COSMOZ stations were first collected and complemented with a wide range of satellite and environmental variables retrieved through GEE, including SM products, vegetation indices, LST, meteorological variables, land cover, elevation, and soil properties. All datasets were temporally resampled to a daily resolution and spatially aligned with each in-situ site. Subsequently, the combined dataset underwent a structured processing pipeline that included data cleaning, correlation analysis, feature selection, and the preparation of multiple input formats suitable for tabular models, sequential models, and graph-based spatio-temporal models.

All data samples were first grouped by site identifier and then chronologically ordered based on observation dates. To ensure a strict temporal separation between training and evaluation and to avoid any forward-looking data leakage, an 60/40 split was applied along the temporal dimension for each site. Specifically, the earliest 60% of observations were used for model training, while the remaining 40% of the most recent observations were reserved exclusively for testing. This temporal split strategy guarantees that models are evaluated only on future data relative to the training period, thereby providing a realistic assessment of predictive performance. Three modelling families were trained using the training set, and their performance was evaluated using the testing set to forecast SM across multiple lead times (1, 3, 5, 7, 10, and 14 days).

The detailed architectures of the sequential and the graph-based spatiotemporal models are presented in the following subsections. For the tabular baseline, an eXtreme Gradient Boosting (XGB) model was employed, representing a state-of-the-art ensemble tree-based method. The XGBoost model was used with its default hyperparameter settings, providing a robust, well-established reference point against which the deep learning and graph-enhanced architectures could be evaluated.

B. GRAPH-TRANSFORMER NETWORK ARCHITECTURE

We propose a novel Graph-Transformer (G-TF) network for SM forecasting, which integrates spatial relationships and temporal dynamics derived from satellite-based data. The model is designed to predict SM at 2 distinct depths including 0–7 cm and 7–28 cm across multiple forecast horizons h = {1,3,5,7,10,14} days. The overall architecture of the proposed model is illustrated in Fig. 4. The proposed G-TF architecture consists of 2 distinct processing pipelines:

1) A temporal sequence processing branch depicted in the right side of Fig. 4, utilizing a standard Transformer encoder block with positional encoding; and
2) A spatial site embedding branch, shown in the left side of Fig. 4, employing a Graph Attention Convolution (GATConv) layer.

The temporal branch extracts dynamic representations from multivariate input sequences using stacked Transformer encoder blocks, which are well-suited for capturing long-range temporal dependencies. In parallel, the spatial branch computes site-level embeddings using a GATConv layer, which models spatial proximity by constructing an adjacency matrix based on geographic coordinates.

We adopted GATConv architecture from [60] to build the site embedding pipeline shown in Fig. 5. In the GATConv layer, the input node features from the adjacency matrix (A) are first linearly transformed using a learnable wight matrix, $W \in \mathbb{R}^{F' \times F'}$, as follows:

$$A' = \alpha A W + b \tag{1}$$

where $A' \in \mathbb{R}^{N \times F'}$ represents the updated node features with F' dimensions, and $b \in \mathbb{R}^{F'}$ is a residual bias term. The matrix α contains the pairwise attention coefficients, α_{ij},

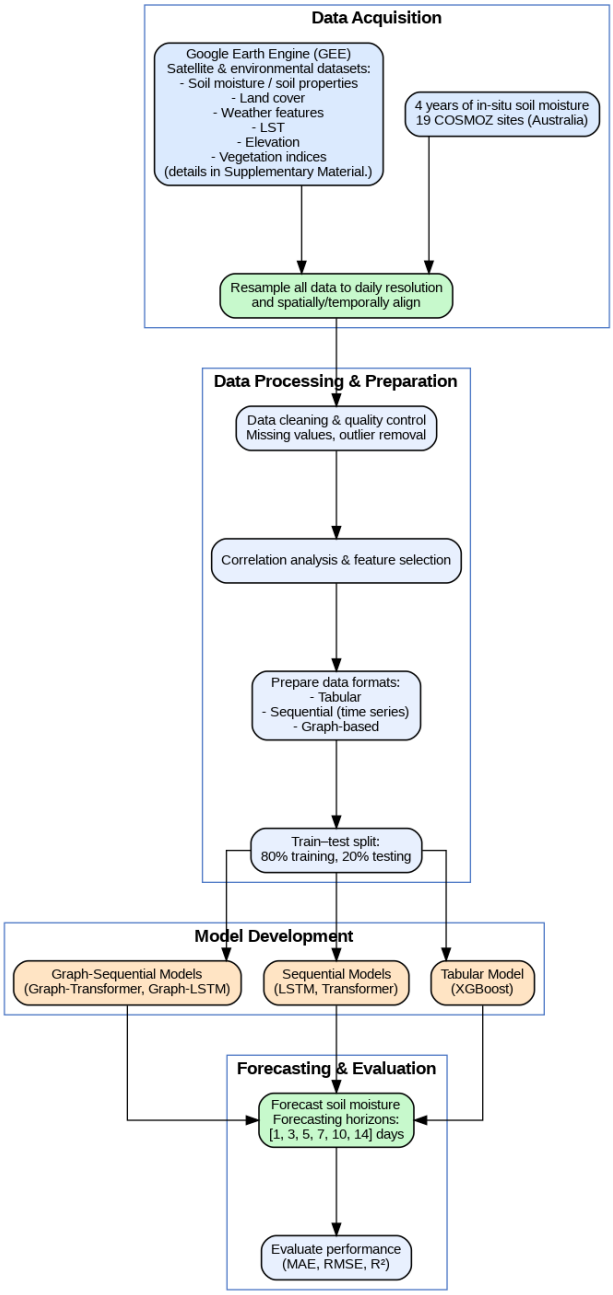

FIGURE 3. Schematic overview of the methodology used for forecasting soil moisture using multimodal remote sensing and in-situ observations. The pipeline includes (i) acquisition of 4 years of in-situ soil moisture from 19 COSMOZ sites across australia and corresponding Google Earth Engine (GEE) datasets, (ii) daily temporal resampling and alignment of all variables, and (iii) data processing, modeling and evaluation steps.

which quantify the importance of node j's features to node i. These coefficients are computed as follows:

$$\alpha_{ij} = \text{softmax}\Big(\text{LeakyReLU}\Big(a^\top \left[Wh_i \,\|\, W\, h_j\right]\Big)\Big) \tag{2}$$

where h_i and h_j are the input features of nodes i and j, respectively; $a \in \mathbb{R}^{2F'}$ is a trainable attention vector; $\|$ denotes concatenation; and LeakyReLU introduces

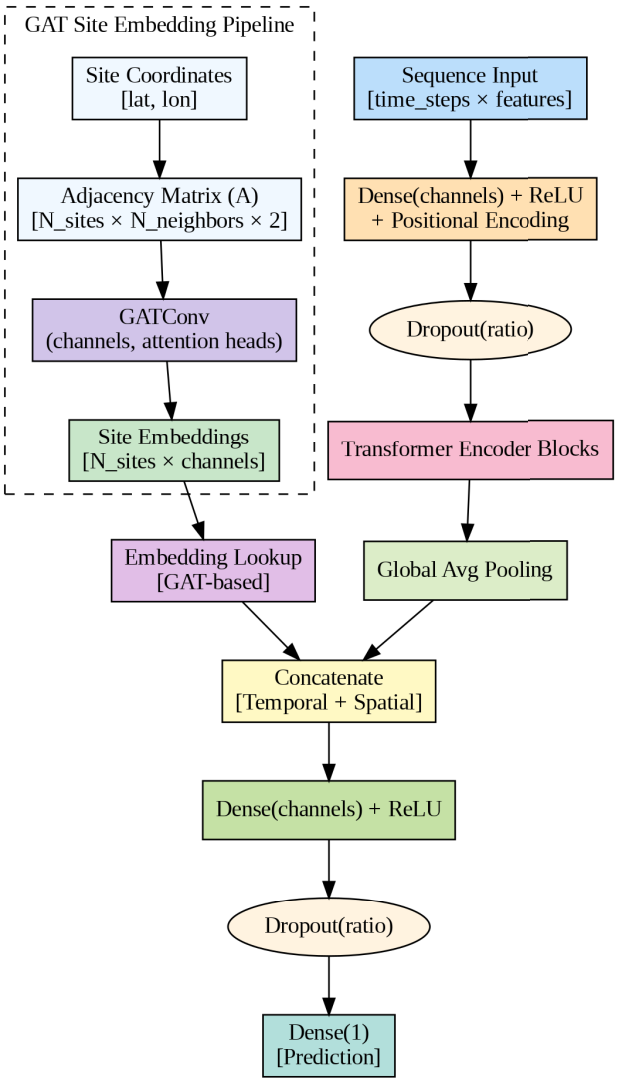

FIGURE 4. Architecture of the proposed graph-transformer model for soil moisture prediction. The pipeline combines spatial site embeddings obtained via a Graph Attention Convolution (GATConv) layer using geographical coordinates and multivariate input sequences.

nonlinearity. The softmax function ensures that the attention scores across all neighbors j of node i are normalized. Dropout is optionally applied to α_{ij} for regularization. Finally, the output representation Z_i for node i is computed by aggregating the transformed features of its neighbors, weighted by the corresponding attention scores:

$$Z_i = \sum_{j \in \mathcal{N}_i} \left(\alpha_{ij}\, A\, W_j\right) + b \tag{3}$$

This aggregation allows the model to learn spatially informed node embeddings. The use of multi-head attention enables the model to capture diverse aspects of the local neighbourhood by attending to multiple representation subspaces. These outputs are then merged via concatenation or averaging to produce the final node embeddings. The spatial and temporal representations are subsequently fused and

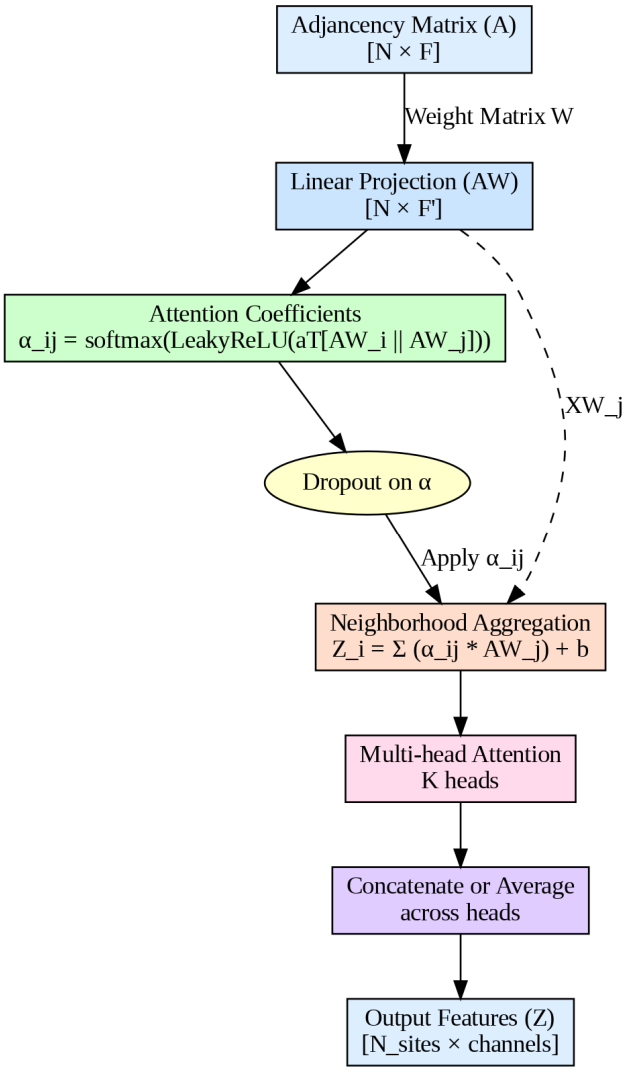

FIGURE 5. Architecture of the GATConv layer used in this study.

passed through fully connected layers to generate SM predictions at the target forecast horizon. Additionally, we introduce a Graph-LSTM (G-LSTM) architecture as an alternative to the proposed G-TF. Although its architecture is not illustrated separately, it closely follows the structure of the G-TF shown in Fig. 4, with the key difference being the substitution of the Transformer encoder block with an LSTM block for temporal sequence modelling. Moreover, the G-LSTM model omits the positional encoding and global average pooling components used in the Transformer's temporal branch. Detailed descriptions of both the Transformer and LSTM models are provided in the following section.

C. BASELINE MODELS FOR COMPARISON

To evaluate the effectiveness of the proposed G-TF model, we compare its performance against three widely used baseline models: XGB, LSTM, and Transformer (TF). Each of these models represents a distinct class of learning approaches, ranging from gradient-boosted decision trees to deep learning methods for sequential data. The details of each baseline model are described below. XGB [61] is a scalable and efficient implementation of gradient-boosted decision trees widely used for regression and classification tasks. It iteratively builds an ensemble of decision trees, where each subsequent tree aims to correct the errors of its predecessors by optimizing a regularized objective function. In this study, XGB serves as a strong non-sequential baseline model, leveraging its ability to handle nonlinear relationships and interactions among input features for SM forecasting. LSTM networks are a type of RNNs designed to effectively capture long-range temporal dependencies in sequential data by mitigating the vanishing gradient problem through gated memory cells [62]. In this study, the LSTM model processes multivariate time series inputs of SM and auxiliary variables to model temporal dynamics and forecast SM at future horizons. Its capability to learn temporal patterns makes it a strong baseline for sequential forecasting tasks. Fig. 6 presents the architecture of the LSTM-based model employed for SM prediction. The model receives an input sequence of shape (T,F), where T is the number of time steps and F the number of features. The sequence is passed through an LSTM layer, which captures temporal dependencies by maintaining an internal memory of prior states. The LSTM outputs are fed into a dense layer to transform the learned representation, followed by a dropout layer to mitigate overfitting. Finally, a fully connected output layer returns the estimated SM value. For detailed information and mathematical formulations of the LSTM layer, readers are referred to [62].

The Multihead Attention Transformer architecture, introduced by Vaswani et al. in 2017 [24], provides a powerful framework for capturing complex dependencies within sequential data. Positional encoding is employed to preserve the order of the input sequence, which is essential since the attention mechanism itself is permutation-invariant. By utilizing multiple attention heads, the model can attend to different parts of the sequence in parallel, thereby learning richer and more diverse contextual representations. A final global average pooling layer aggregates these learned features across the sequence dimension, producing a fixed-size representation. This combination of components achieves a balance between expressive capacity and computational efficiency, making the architecture highly effective for a wide range of sequence-based tasks, including natural language processing, image analysis, and time series forecasting. Fig. 7 illustrates the architecture of the Transformer-based sequence model used for SM forecasting in this study. The model accepts an input sequence with shape (T, F), where T denotes the number of time steps and F the number of features. The input is first passed through a fully connected (dense) layer and a dropout operation to reduce overfitting. Sine-based positional encoding is then added to the transformed input to preserve temporal order. The resulting sequence is processed by a stack of Transformer encoder blocks, each comprising multi-head self-attention (MHA) and feedforward network (FFN) sublayers. A global average pooling layer aggregates the

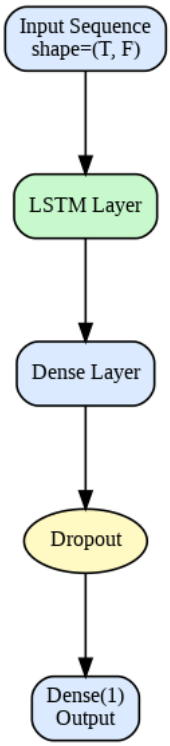

FIGURE 6. Architecture of the LSTM model used as a baseline in this study.

temporal dimension, followed by dense layers and additional dropout, leading to a final scalar output representing the predicted SM value. This architecture enables the model to effectively capture both short-term temporal patterns and long-range dependencies. For additional details on positional encoding and the MHA architecture, readers are referred to [24].

IV. RESULTS

A. EXPERIMENTAL SETUP

To ensure temporal consistency across heterogeneous RS datasets, all variables were resampled to a daily resolution. Spatially, a site-based extraction strategy was employed, in which each variable was sampled at its native spatial resolution from the pixel overlapping or nearest to the geographic coordinates of each in-situ station. This approach allowed for the spatial matching of RS data to the footprint of the in-situ measurements. The in-situ SM data, derived from cosmic-ray neutron probes, represent an average over an area of approximately 30*ha*. In contrast, the RS variables vary in spatial resolution, ranging from 10 m for Sentinel-1 to 27 km for GLDAS. To reduce feature redundancy and avoid multicollinearity in the integrated dataset, pairwise Pearson correlation coefficients (R) were computed among all variables. Highly correlated feature pairs with absolute R greater than 0.90 were identified, and from each pair, the feature exhibiting the lower correlation with the in-situ SM was removed. This dimensionality reduction step ensured

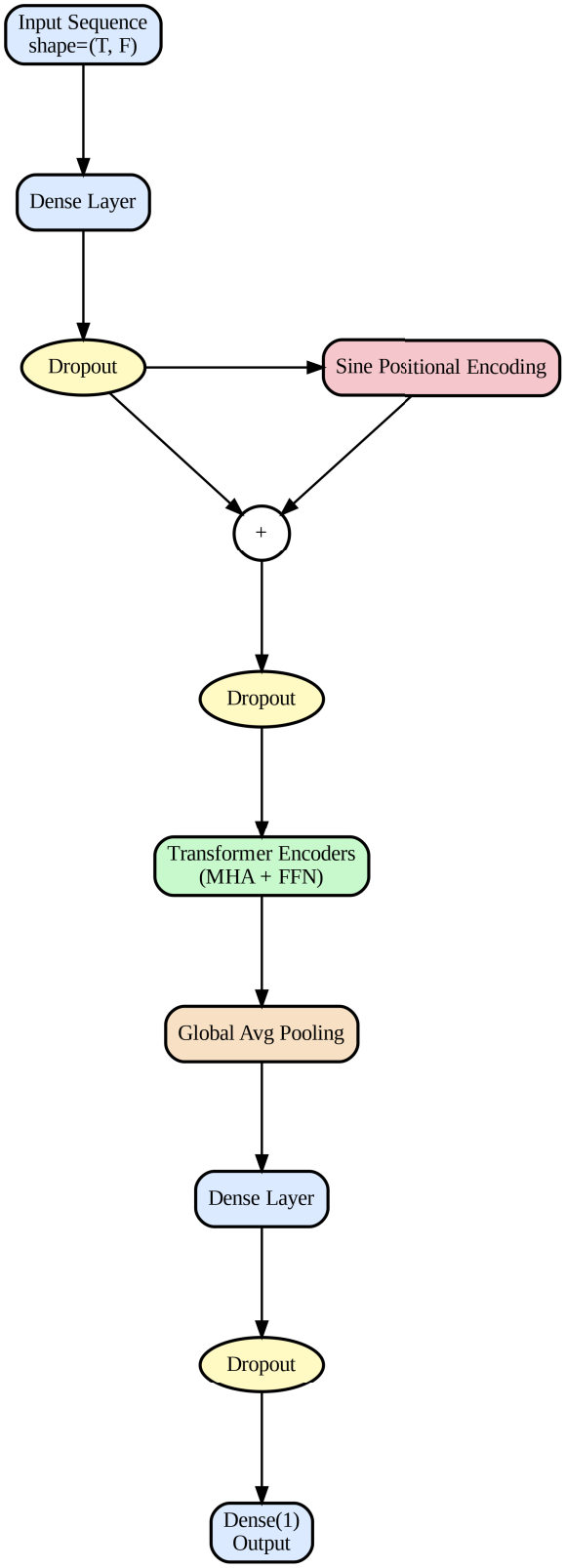

FIGURE 7. Architecture of the transformer model used as a baseline in this study.

that the model inputs retained only the most relevant and non-redundant information. For each site, 60% of

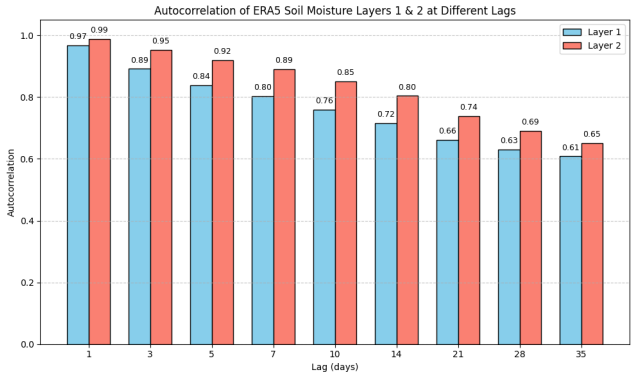

FIGURE 8. Lagged autocorrelation analysis of ERA5 volumetric soil moisture for layer 1 and layer 2 across all sites. Autocorrelations were computed after forward and backward imputation within each site to preserve temporal continuity.

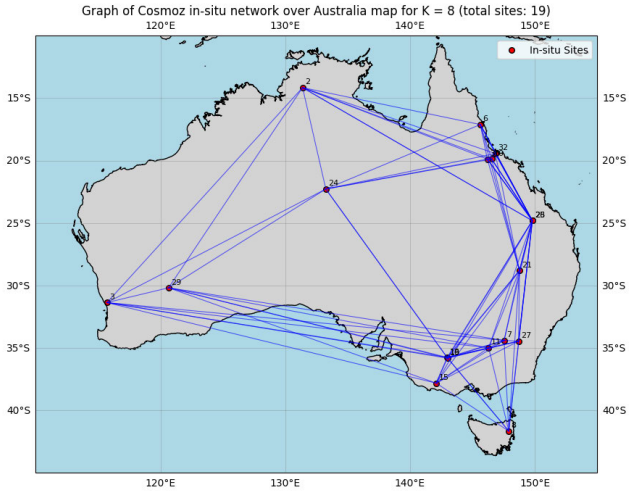

FIGURE 9. Visualization of the spatial graph constructed over the CosmOz in-situ soil moisture monitoring network using K-nearest neighbours ($K = 8$). To see site names based on their numbers, refer to Table 2 II.

the data, ordered temporally, was used for training, while the remaining 40% was reserved for testing the models. For the sequential models, we evaluated lag intervals of [1, 3, 5, 7, 14, 21, 28, 38] days to identify the optimal input sequence length. The best performance was achieved with a timestep of 7 days. As shown in Fig. 8, the autocorrelation of soil moisture in both layers 1 and 2 remains above 0.8 for up to 7 lag days. Furthermore, Fig. 8 illustrates how short- and medium-term memory differs between the 2 soil layers, with layer 2 typically exhibiting higher persistence over longer lags.

During model development, we evaluated multiple graph construction strategies and node attribute configurations. Specifically, adjacency matrices were derived using different criteria, including distance-based, correlation-based, and KNN-based graphs, and node attributes were constructed from both comprehensive site-related features (e.g., soil properties, land cover, and elevation) and geographic coordinates. Across all evaluated configurations, the KNN-based graph constructed using geospatial coordinates consistently achieved the best predictive performance and training stability. However, to maintain conciseness and to focus the main analysis on comparing graph-based and non-graph-based modeling paradigms rather than alternative graph construction techniques, only results corresponding to the best-performing geospatial KNN graph are reported in the main manuscript. Detailed comparative results for different graph construction strategies are provided in Fig. S-1 in the Supplementary Material.

To determine the optimal number of nearest neighbours (k) for the graph-based models, we evaluated values of k ranging from 3 to 11. The best performance was achieved with $k = 8$. Fig. 9 illustrates the resulting graph structure constructed over the CosmOz network.

For the XGB model, default parameter values were used during training. In contrast, the Transformer and LSTM models were tuned using Optuna [63], an automated hyperparameter optimization framework, to identify their optimal configurations. To ensure a fair comparison, the same optimized parameters were applied to the corresponding graph-based models including G-TF and G-LSTM. A comprehensive list of all model parameters is provided in Table-S2 in the Supplementary Materials. We employed 3 widely used standard metrics to evaluate model performance including the coefficient of determination (R^2), Mean Absolute Error (MAE), and Root Mean Square Error (RMSE), as defined below:

$$R^2 = 1 - \frac{\sum_{i=1}^{N}(y_i - \hat{y}_i)^2}{\sum_{i=1}^{N}(y_i - \bar{y})^2} \tag{4}$$

$$\text{MAE} = \frac{1}{N}\sum_{i=1}^{N}\left|y_i - \hat{y}_i\right| \tag{5}$$

$$\text{RMSE} = \sqrt{\frac{1}{N}\sum_{i=1}^{N}(y_i - \hat{y}_i)^2} \tag{6}$$

where y_i represents the observed ground-truth value, $\hat{y}_i$ denotes the predicted value from the model, $\bar{y}$ is the mean of the observed values, and N corresponds to the total number of samples. R^2 indicates how well the model captures the variability in the data, while MAE and RMSE evaluate the prediction accuracy by measuring the average and squared deviations between predicted and observed values, respectively.

B. COMPARISON ACROSS FORECAST HORIZONS

To investigate model robustness across different forecasting horizons, we analysed prediction performance as a function of time horizon (h), using 3 evaluation metrics including R^2, MAE, and RMSE. For each model, metric values were averaged across all the study sites to reflect consistency. The results are shown in Fig. 10 for models in layers 1 and 2 across various forecast horizons. In general, model performance deteriorates with increasing forecast horizon.

However, the proposed G-TF consistently outperforms other models, across 1- to 10-day forecasts for layer 1, and across all horizons for layer 2. The LSTM and G-LSTM models exhibited the poorest performance across both layers and all forecast horizons, except for the 14-day horizon ($h = 14$) at layer 1, where G-LSTM achieved slightly improved results in terms of both R^2 and RMSE.

To quantify the benefit of incorporating spatial relationships through graph-based modelling, we computed the percentage improvement of the G-TF and G-LSTM models over their respective baseline models including TF and LSTM for each forecast horizon at both layers. As shown in Fig. 11, the G-TF consistently outperforms the baseline TF, achieving improvements of up to 10% in R^2 and 8% in RMSE at a 5-day forecast horizon ($h = 5$) for layer 1, and up to 11% in R^2 and 9% in RMSE at a 14-day horizon ($h = 14$) for layer 2.

However, G-LSTM exhibited a different performance pattern compared to its baseline. It underperformed relative to the original LSTM model at the 3-day forecast horizon ($h = 3$) for layer 1 and at the 10-day horizon ($h = 10$) for layer 2. These results suggest that incorporating spatial dependencies via graph structures does not consistently benefit LSTM models for short-term forecasting in layer 1 or long-term forecasting in layer 2. Nevertheless, G-LSTM outperformed the standard LSTM across most other forecast horizons. Specifically, for layer 1, G-LSTM achieved the highest R^2 improvement of up to 14% at $h = 14$ days and the greatest RMSE reduction of up to 7% at $h = 5$ days. In layer 2, the maximum improvements were observed at $h = 5$ days, with gains of up to 6% in R^2 and 5% in RMSE.

C. COMPARISON ACROSS STUDY SITES

To evaluate the generalization capacity and stability of each model across diverse spatial domains, we computed all the selected performance metrics including R^2, MAE, and RMSE per site and model, averaged over all forecast horizons (1, 3, 5, 7, 10, 14 days). Outlier values were removed using the inter-quartile range (IQR) method to ensure a fair comparison. Fig. 12 presents the distribution of these metrics in the form of box plots for both layer 1 and layer 2. These plots reveal the relative performance of each model across spatially distributed sites and highlight key differences in central tendency and variance. Overall, the proposed G-TF model demonstrated lower error dispersion and higher median R^2 values, indicating better consistency and predictive reliability across ecologically diverse regions.

Among all models, the standard TF exhibited the closest performance to the proposed G-TF. Nevertheless, G-TF consistently outperformed TF at both soil layers across the study sites. Specifically, G-TF achieved approximately 0.4 and 0.6 in median R^2 at layers 1 and 2, respectively, representing an improvement of about 0.1 at both layers over the baseline TF model. Additionally, G-TF demonstrated superior performance in terms of error metrics, yielding approximately 8% lower median MAE and 4% lower median RMSE across sites in both layers compared to the standard TF model. Across all models, performance in layer 2 consistently surpasses that of layer 1, with higher R^2 values, lower MAE and RMSE, and overall greater robustness as evidenced by reduced variability around the median. For instance, the G-TF model achieves an average R^2 of up to 0.6 in layer 2, compared to less than 0.4 in layer 1. The IQR for R^2 in layer 2 is approximately 0.2, roughly 30% narrower than the 0.3 IQR observed in layer 1, indicating more stable performance. In terms of error metrics, G-TF yields median MAE and RMSE values of approximately 0.040 m^3/m^3 and 0.055 m^3/m^3, respectively, in layer 1. In contrast, these values drop to around 0.025 m^3/m^3 and 0.036 m^3/m^3 in layer 2, reflecting more than a 30% reduction in prediction errors at both metrics across the study sites.

For a more detailed site-level evaluation, including per-site performance metrics for all models and the identification of sites where predictive skill is limited or graph-based augmentation yields marginal improvements, the reader is referred to Table S-3 in the Supplementary Materials.

D. COMPARISON ACROSS LAND COVERS

To assess the spatial consistency of the proposed G-TF model, we evaluated model performance across different land cover types using the MODIS land cover classification. MAE was computed for each model, aggregated within individual land cover classes. The results are visualized in radar plots in Fig. 13, showing MAE distributions across land cover types for both SM layers. Overall, G-TF consistently outperformed all baseline models across most land cover categories. The only exception was the Open Shrubland category, where G-TF and G-LSTM achieved comparable performance at both SM layers. This result highlights the spatial robustness of G-TF across diverse land surface types and suggests its strong generalization capability in heterogeneous environments.

E. COMPARISON ACROSS SEASONS

To investigate model behavior under more practical and environmentally realistic conditions, we conducted a seasonal performance analysis across different soil depths. Fig. 14 presents a comparative evaluation of model performance across four seasons for both shallow (Layer 1) and deeper (Layer 2) SM predictions. The results reveal clear seasonal variability, with all models generally exhibiting higher prediction errors during hydrologically dynamic periods (e.g., Summer/Spring), while achieving more stable performance during colder or wetter seasons (e.g., Winter/Autumn). Notably, the proposed G-TF model demonstrates consistently strong performance across seasons and soil layers, indicating enhanced robustness to seasonal changes compared to other models.

In addition, the comparison between Layer 1 and Layer 2 highlights depth-dependent performance differences, reflecting the distinct physical processes governing near-surface and subsurface SM dynamics. While deeper layers tend to exhibit smoother temporal variations and

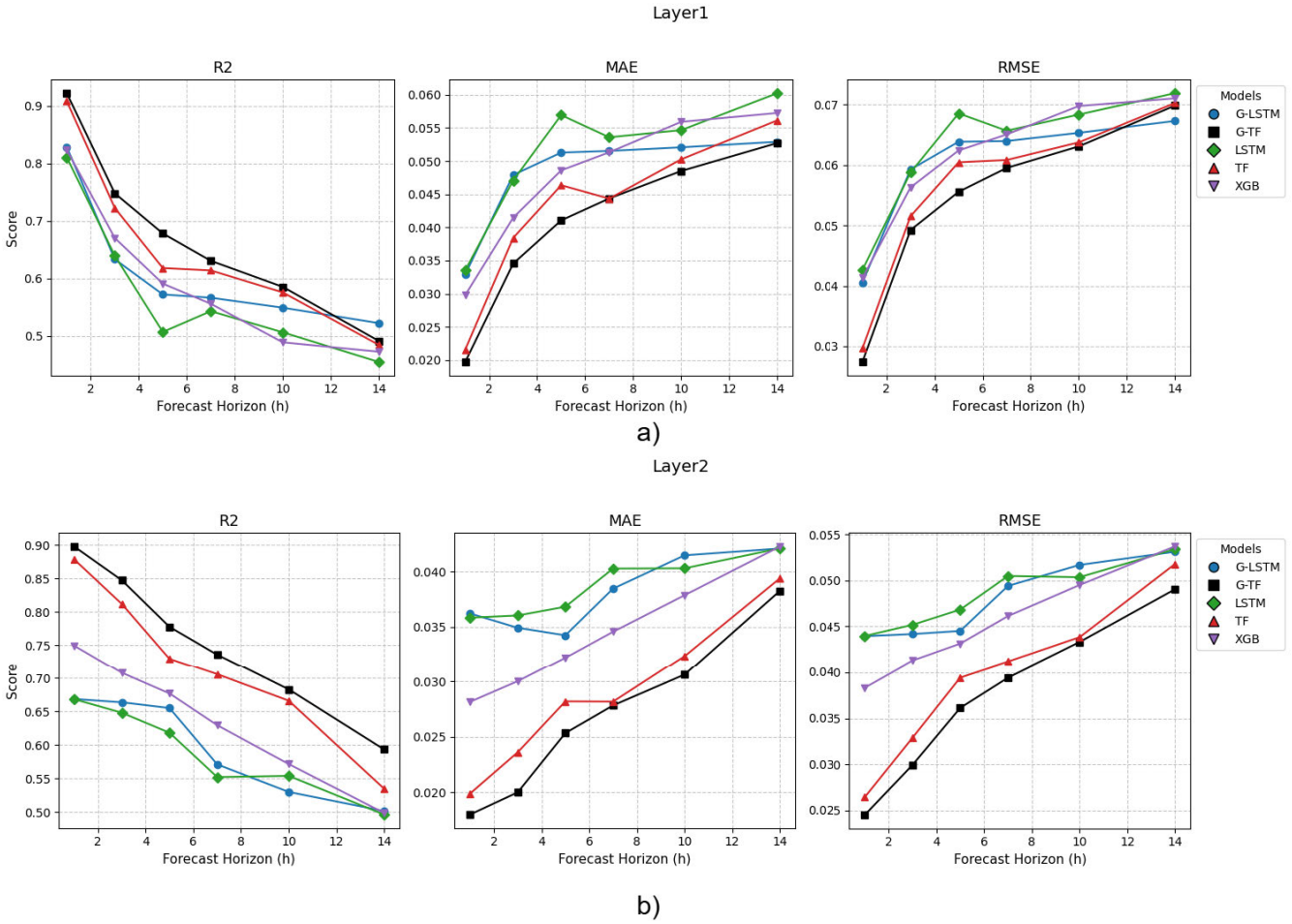

FIGURE 10. Forecast performance of different models across varying prediction horizons (h) for a) layer 1 and b) layer 2. Each subplot summarizes the mean of R^2, MAE, and RMSE over all evaluation sites for each model. Forecast horizons span from short-term to longer-term predictions. The G-TF model is highlighted in black to emphasize its comparative performance across time steps.

lower seasonal volatility, the relative performance ranking of models remains largely consistent across depths. This suggests that the proposed architecture effectively captures shared spatial–temporal patterns across soil layers. These findings provide practical insights into the seasonal reliability and depth-wise generalization capability of the proposed model in real-world SM monitoring scenarios.

F. RELATIVE FEATURE IMPORTANCE

To interpret the feature contribution to prediction performance, we conducted a permutation importance analysis for the proposed G-TF model on layer 1 and layer 2 outputs. Each input feature was individually permuted across all time steps in the input sequence, and the increase in RMSE was measured relative to the baseline. As shown in Fig. 15, this method reveals the most influential variables in the multimodal input space. Differences between the 2 layers also suggest how feature relevance may shift depending on model depth.

In layer 1, the most influential predictor is soil temperature at layer 2, indicating a strong vertical coupling between root-zone thermal conditions and SSM. Following this, rainfall and wind speed emerge as the second and third most important contributors, albeit with significantly lower positive impacts. On the other hand, among the negatively contributing features, surface pressure and total precipitation are the most influential in layer 1 SM forecasting. Interestingly, the pattern is nearly reversed in layer 2. Surface pressure and total precipitation become the most positively influential features, while soil temperature at layer 2, wind speed, and rainfall exhibit strong negative contributions. This contrast suggests a depth-dependent shift in the influence of meteorological and surface variables, likely reflecting the distinct dynamics governing SMM and RZSM. Additionally, the contributions of different features are more evenly distributed in layer 2 compared to layer 1, indicating a more balanced influence of input variables on RZSM predictions.

V. DISCUSSIONS

The empirical results presented in this study provide strong evidence that incorporating spatial dependencies via graph-based modelling can enhance SM forecasting performance, particularly when fused with attention-based

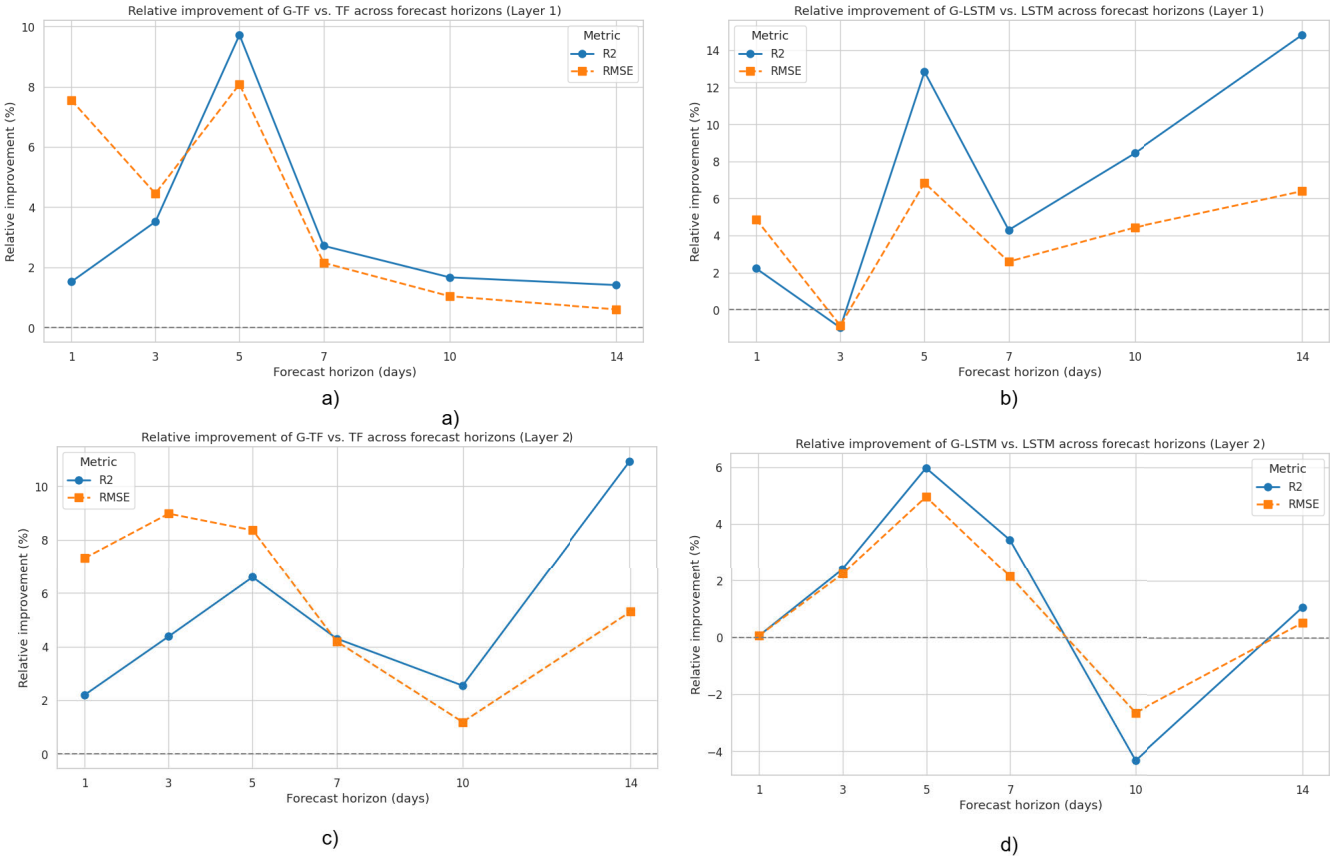

FIGURE 11. Relative improvement (%) of graph-augmented models (G-TF and G-LSTM) over their baselines (TF and LSTM) across multiple forecast horizons (h). Plots show the percent change in R^2 and RMSE for a), b) layer 1 and c), d) layer 2 soil moisture predictions. Positive values indicate enhanced performance.

temporal architectures. Across all evaluation dimensions including forecast horizon, spatial distribution, and land cover heterogeneity, the proposed G-TF model consistently outperformed baseline deep learning models, indicating superior generalization capacity and robustness in spatiotemporal prediction tasks.

A. FORECAST HORIZON SENSITIVITY AND TEMPORAL GENERALIZATION

As shown in Fig. 10, the performance of all models declined as forecast horizons extended, a trend commonly observed in environmental time series prediction due to increasing uncertainty and error accumulation over time. However, the G-TF model demonstrated more robustness across horizons. Notably, it preserved a consistent performance advantage over the baseline TF from short (1-day) to extended (14-day) horizons for both soil layers (Fig. 11). This indicates that the incorporation of spatial context not only enhances short-term precision but also helps mitigate error propagation in longer-term forecasts. The most significant gains were observed at intermediate to long horizons including 5- and 14-day forecasts, where the G-TF achieved improvements of up to 10–11% in R^2 and 8–9% in RMSE. This suggests that graph-based spatial encoding may provide complementary contextual information that compensates for the diminishing utility of temporal signals at longer lead times. In contrast to G-TF, the performance of the G-LSTM model was less consistent and did not exhibit the same level of improvement over its baseline. While G-LSTM benefited from spatial augmentation at several horizons, its gains were less consistent and, in some cases, performance degraded relative to the standard LSTM. This may be attributed to the inherent sequential bottlenecks in LSTM architectures, which may be less capable of integrating parallel spatial information, especially when temporal dependencies are already challenging to capture [24]. In contrast, the Transformer-based models, particularly G-TF, more effectively leveraged graph-encoded features due to their non-recurrent structure and global attention mechanisms, making them better suited for simultaneous spatiotemporal fusion.

B. CROSS-SITE EVALUATION AND SPATIAL ROBUSTNESS

Analysis of model performance across the 19 geographically distributed sites further reinforced the effectiveness of the G-TF as illustrated in Fig. 12. Compared to TF, the G-TF exhibited higher median R^2 values and lower error dispersion,

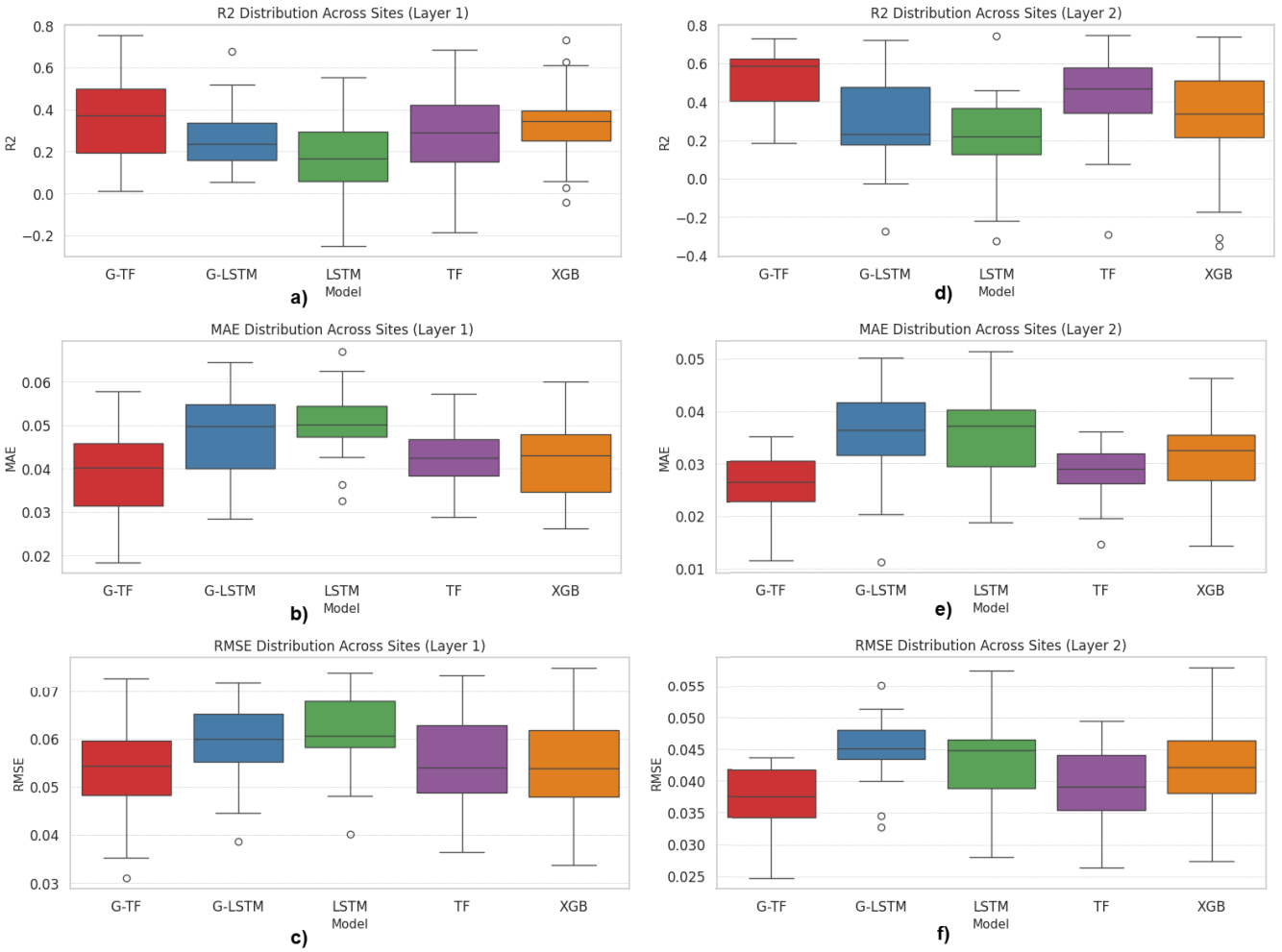

FIGURE 12. Distribution of prediction performance metrics (R^2, MAE, and RMSE) across all sites for different models at a), b), c) for layer 1 and d), e), f) for layer 2.

especially in layer 2, where median R^2 reached 0.6 with IQR reduced by 30% relative to layer 1. The narrowed IQR and reduced error metrics including MAE and RMSE indicate that the G-TF generalizes more reliably across diverse climatic and topographic conditions, offering consistent predictive performance rather than relying on favourable local conditions. Layer-wise comparisons revealed that SM predictions at deeper layers were generally more stable and accurate than those at the surface layer. This is likely due to the stronger buffering effect of root-zone processes and a higher degree of persistence in deeper soil layers [64]. The G-TF was particularly effective at capturing these dynamics, achieving median RMSE values as low as 0.036 m^3/m^3 in Layer 2, compared to approximately 0.055 m^3/m^3 in Layer 1. These findings emphasize the value of spatially informed temporal models for capturing slower and more complex hydrological processes at depth.

C. LAND COVER GENERALIZATION

The radar plots shown in Fig. 13 evaluating MAE across MODIS land cover types revealed that G-TF achieved the lowest errors across most categories, highlighting its capacity to generalize beyond specific terrain or vegetation types. The only exception was the Open Shrubland class, where G-TF and G-LSTM exhibited comparable performance. This could reflect unique soil-vegetation-atmosphere interactions in such semi-arid environments, where localized factors like microtopography and sparse vegetation cover may introduce variability that is less well captured by spatial graphs based solely on geodesic proximity [65].

D. FEATURE IMPORTANCE AND DEPTH-SPECIFIC DYNAMICS

Permutation-based feature importance analysis illustrated in Fig. 15 provided valuable insights into the underlying mechanisms driving the G-TF's predictions. In layer 1, soil temperature from layer 2 was the dominant positive contributor, suggesting strong vertical coupling and the relevance of root-zone thermal inertia for near-surface moisture dynamics. Rainfall and wind speed also contributed positively, reflecting their direct physical roles in soil-atmosphere interactions. In contrast, for layer 2, surface pressure and total precipitation

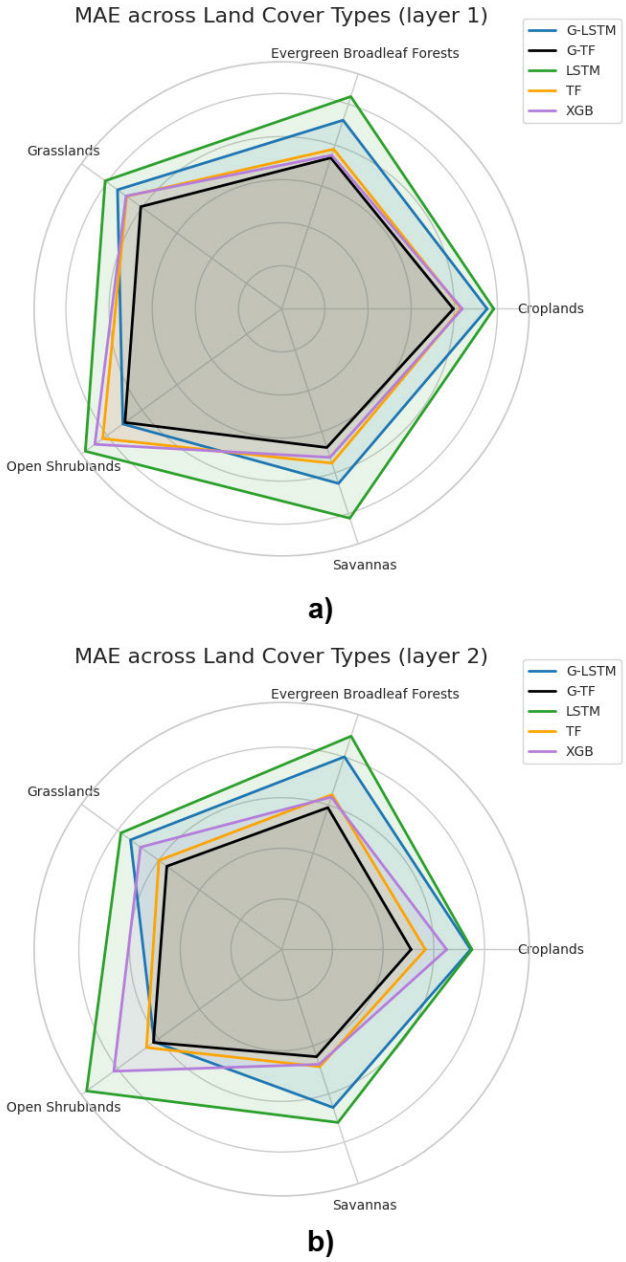

FIGURE 13. Radar charts illustrating the Mean Absolute Error (MAE) of different models across various land cover types for a) layer 1 and b) layer 2.

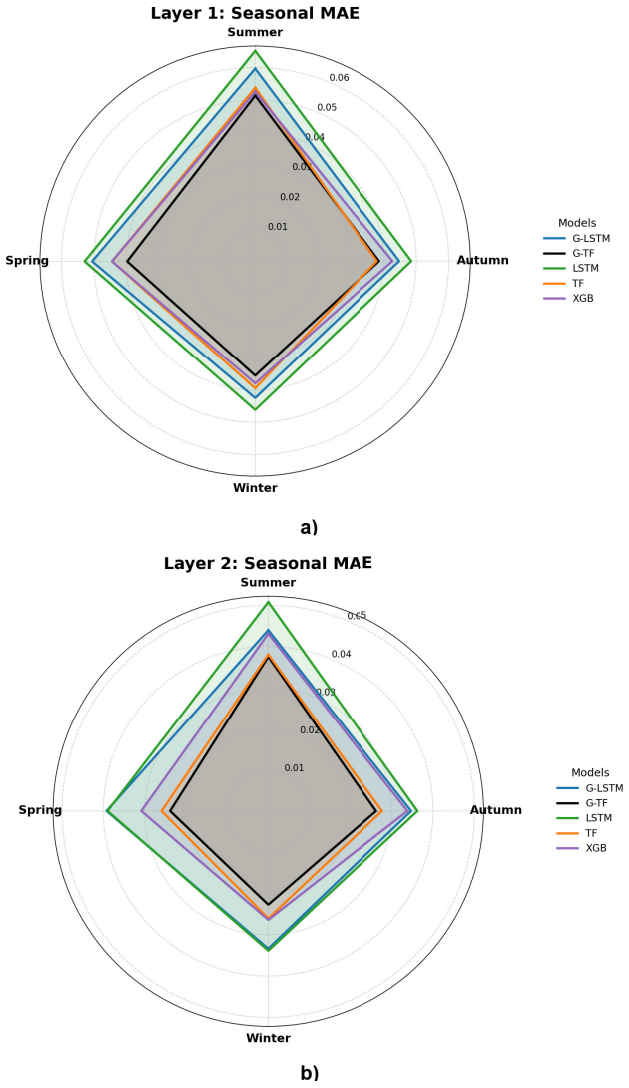

FIGURE 14. Seasonal performance comparison of different models for soil moisture prediction at (a) Layer 1 and (b) Layer 2 using mean absolute error (MAE).

emerged as the most influential features, indicating that broader-scale meteorological and hydrological processes dominate RZSM regulation. Additionally, the influence of individual features was more balanced in layer 2, suggesting that the model draws upon a more diverse and distributed set of predictors when estimating deeper SM. This could be due to the integrative nature of root-zone processes, where moisture retention, capillary rise, and deep percolation involve multiple interacting variables [66]. Furthermore, the shift in feature polarity between layers like surface pressure switching from negative to positive influence underscores the depth-dependent nature of soil water dynamics and validates the need for differentiated modelling strategies at different soil depths.

E. TRAINING TIME ANALYSIS

The average training times across all horizons for the evaluated models are illustrated in Figure 16, providing insight into the computational demands of each approach. **GAT-TF-Layer2** exhibits the highest training time (∼524 s), followed closely by **GAT-TF-Layer1** (∼461 s), indicating that incorporating graph attention with Transformer layers substantially increases computational cost. Standard Transformer models (**TF-Layer1** and **TF-Layer2**) also show high training times (∼357–364 s), reflecting the complexity of attention-based sequence modeling. LSTM-based models have moderate training times, ranging from ∼153 s (**LSTM-Layer1**) to ∼213 s (**LSTM-Layer2**), suggesting that recurrent architectures are less computationally intensive

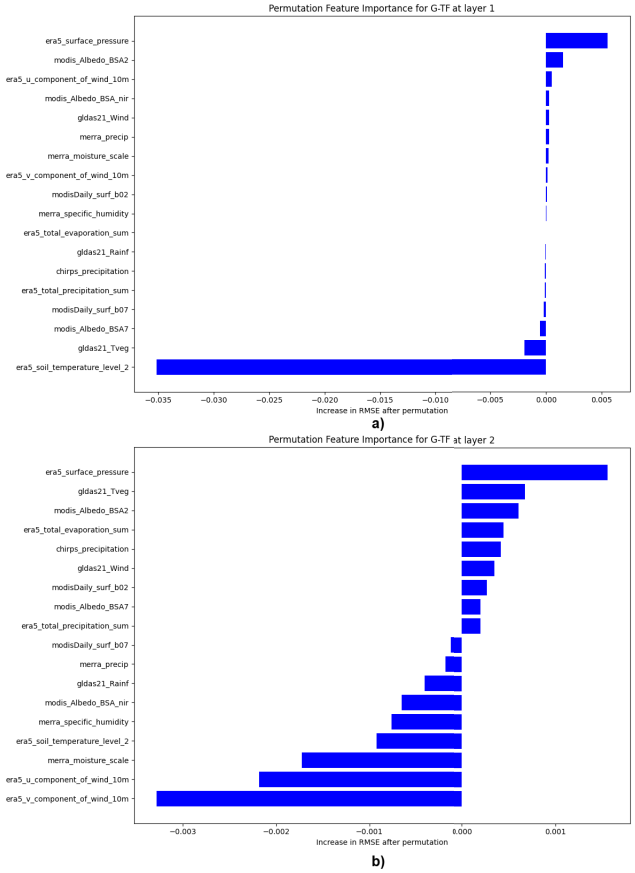

FIGURE 15. Permutation feature importance for the proposed G-TF model at forecast horizon of 1 day in a) layer 1 and b) layer 2 using RMSE-based scoring. Each bar represents the average increase in RMSE over 3 permutations when a feature is randomly shuffled across all time steps, reflecting its impact on model performance. Features with higher values are more influential for soil moisture prediction at the target horizon.

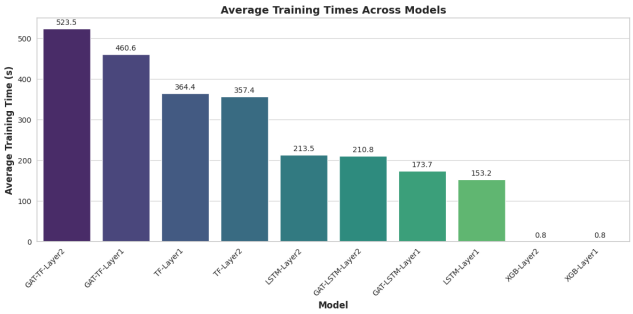

FIGURE 16. Average training times (in seconds) for different models across all horizons. Models incorporating graph attention (GAT-TF and GAT-LSTM) exhibit the highest training times, followed by standard transformer and LSTM models, while XGBoost models are significantly faster. The plot highlights the computational cost differences associated with model complexity.

than Transformers with graph attention but still slower than gradient boosting models. In contrast, **XGB** models are extremely efficient (∼0.8 s), demonstrating their suitability for rapid prototyping or scenarios where training time is critical. Overall, the figure highlights the trade-off between model complexity and training efficiency, which should be considered when selecting models for large-scale applications. All training times were recorded using the Google Colab free version, equipped with a NVIDIA T4 GPU, 12 GB RAM, and standard Colab CPU resources.

F. POTENTIAL LIMITATIONS

Despite the strong and consistent performance of the proposed Graph–Transformer model, several sources of uncertainty and methodological limitations should be acknowledged to ensure scientific transparency and to contextualize the reported results.

First, scale mismatch between in-situ and RS observations remains an inherent source of uncertainty. The cosmic-ray neutron probe measurements represent an effective footprint of approximately 30 ha, whereas the spatial resolution of the RS inputs ranges from tens of meters (Sentinel-1) to several tens of kilometers (e.g., GLDAS). Although a site-based pixel extraction strategy was adopted to minimize spatial mismatch, this approach cannot fully resolve sub-pixel heterogeneity in soil properties, vegetation structure, or topography. Consequently, part of the residual error particularly in surface SM may be attributed to representativeness differences rather than model inadequacy.

Second, temporal resampling and data imputation introduce additional uncertainty. All variables were resampled to a daily resolution to ensure temporal alignment, and forward/backward imputation was applied to preserve continuity for sequential modeling. While this is a common and necessary practice in multimodal Earth observation studies, it may smooth short-term variability and attenuate extreme events, especially for variables originally available at coarser temporal resolutions. This limitation is likely more pronounced at shorter forecast horizons and in hydrologically dynamic periods, such as during intense rainfall or rapid drying phases.

Third, the graph construction strategy relies exclusively on geospatial proximity, implemented via a K-nearest neighbour (KNN) graph based on latitude and longitude. Although this choice yielded the most stable and accurate results among the evaluated configurations, it implicitly assumes that spatial closeness is a sufficient proxy for hydrological similarity. In reality, SM dynamics are also influenced by non-local factors such as soil texture, land management practices, subsurface connectivity, and climatic gradients. As a result, some physically meaningful long-range dependencies may not be fully captured by a distance-based graph alone, particularly in heterogeneous or topographically complex regions.

Fourth, model generalization is constrained by the spatial extent and density of the monitoring network. The study is based on 19 sites within the CosmOz network, which, while geographically distributed, may not fully represent all climatic regimes, soil types, or land management conditions encountered at continental or global scales. Although cross-site evaluation demonstrates strong spatial robustness

within the study domain, performance may differ when applied to regions with substantially different hydro-climatic characteristics or data availability.

Fifth, uncertainty quantification is not explicitly modeled in the current framework. The evaluation focuses on deterministic point predictions assessed using standard performance metrics (e.g., R^2, MAE, RMSE). While these metrics effectively quantify average predictive accuracy, they do not capture predictive uncertainty or confidence intervals, which are critical for operational decision-making in hydrology and agriculture. Incorporating probabilistic forecasting or Bayesian deep learning approaches could provide more informative uncertainty estimates in future work.

Finally, the increased computational complexity of graph-based Transformer models represents a practical limitation. As shown in the training time analysis, graph-augmented attention architectures require substantially higher computational resources compared to traditional ML models such as XGBoost. This trade-off between accuracy and efficiency may limit scalability in real-time or resource-constrained operational settings, particularly as the number of sites or graph nodes increases.

Overall, while these limitations do not undermine the comparative advantages demonstrated by the proposed approach, they highlight important directions for future research. Addressing scale mismatch, enriching graph construction with physical attributes, expanding spatial coverage, and incorporating uncertainty-aware modeling frameworks will further strengthen the reliability and applicability of graph-based spatiotemporal models for SM forecasting.

VI. CONCLUSION

This work introduced a Graph-Transformer architecture that explicitly integrates spatiotemporal dependencies for soil moisture forecasting across multiple sites and soil depths. While conventional Transformer models have demonstrated strong performance in capturing long-range temporal dependencies, their inability to model spatial correlations across geographically distributed sites limits their applicability in large-scale environmental prediction tasks. To overcome this challenge, we constructed a hybrid deep learning framework that incorporates graph neural networks to encode site-specific spatial relationships based on geolocation attributes, and Transformer encoders to model sequential dependencies in daily RS time series. Our experiments, conducted using a comprehensive dataset comprising 4 years of daily multimodal RS data from 19 sites across Australia, demonstrate the efficacy of the proposed model in forecasting surface (0–7 cm) and root-zone (7–28 cm) soil moisture. Quantitative results indicate that the Graph-Transformer yields up to 10–11% improvement in R^2 and 8–9% reduction in RMSE compared to the baseline Transformer across both depths. Furthermore, the Graph-Transformer outperforms all baseline models including LSTM, XGB, and standalone Transformer across the study sites, highlighting its consistent generalization across heterogeneous geographic and climatic conditions. These performance gains show the model's ability to capture both spatial correlations and long-term temporal dynamics, which are essential for accurately modelling soil water variability driven by complex interactions among meteorological, geophysical, and topographical factors. Its demonstrated superiority in soil moisture forecasting has direct implications for operational drought monitoring, water resource management, and precision agriculture. Future work may focus on improving model generalization to unseen regions by expanding the training dataset and incorporating additional data sources. Integrating more soil physical attributes and geospatial information into the graph construction process could further support learning. Prior studies [67], [68], [69] have demonstrated that physics-informed ML approaches can substantially enhance performance, particularly in challenging settings such as sparse datasets and extreme value conditions.

ACKNOWLEDGMENT

The authors would like to thank Google Earth Engine for providing access to a wide range of satellite and remote sensing datasets used in this study. They also would like to thank the CosmOz network for supplying in-situ soil moisture data across the study sites in Australia.

DATA

This study utilizes publicly available datasets. All satellite-based and in-situ soil moisture datasets employed in this work can be accessed and downloaded from their respective official repositories. Detailed descriptions and references to each dataset are provided at Table-S1 in Supplementary Materials.

REFERENCES

[1] S. I. Seneviratne, T. Corti, E. L. Davin, M. Hirschi, E. B. Jaeger, I. Lehner, B. Orlowsky, and A. J. Teuling, "Investigating soil moisture—Climate interactions in a changing climate: A review," *Earth-Sci. Rev.*, vol. 99, no. 3, pp. 125–161, 2010.

[2] L. Samaniego, S. Thober, N. Wanders, M. Pan, O. Rakovec, J. Sheffield, E. F. Wood, C. Prudhomme, G. Rees, H. Houghton-Carr, M. Fry, K. Smith, G. Watts, H. Hisdal, T. Estrela, C. Buontempo, A. Marx, and R. Kumar, "Hydrological forecasts and projections for improved decision-making in the water sector in Europe," *Bull. Amer. Meteorological Soc.*, vol. 100, no. 12, pp. 2451–2472, Dec. 2019.

[3] Q. Zhu, K. Liao, Y. Xu, G. Yang, S. Wu, and S. Zhou, "Monitoring and prediction of soil moisture spatial–temporal variations from a hydropedological perspective: A review," *Soil Res.*, vol. 50, no. 8, pp. 625–637, 2013.

[4] E. H. Hogg, A. G. Barr, and T. A. Black, "A simple soil moisture index for representing multi-year drought impacts on Aspen productivity in the western Canadian interior," *Agricult. Forest Meteorol.*, vols. 178–179, pp. 173–182, Sep. 2013.

[5] X. Liang, H. Gu, Y.-P. Xu, L. Wang, Y. Guo, and L. Liu, "Improvement of physics-based and data-driven model simulations based on multi-source soil moisture datasets," *J. Hydrol., Regional Stud.*, vol. 60, Aug. 2025, Art. no. 102557.

[6] X. Cai, Z.-L. Yang, Y. Xia, M. Huang, H. Wei, L. R. Leung, and M. B. Ek, "Assessment of simulated water balance from noah, noah-MP, CLM, and VIC over CONUS using the NLDAS test bed," *J. Geophys. Res., Atmos.*, vol. 119, no. 24, p. 13, Dec. 2014.

[7] M. Amiri, M. Abolhasan, N. Shariati, and J. Lipman, "RF-self-powered sensor for fully autonomous soil moisture sensing," *IEEE Trans. Microw. Theory Techn.*, vol. 71, no. 3, pp. 1374–1387, Mar. 2023.

[8] R. Keshavarz and N. Shariati, "High-sensitivity and compact time domain soil moisture sensor using dispersive phase shifter for complex permittivity measurement," *IEEE Trans. Instrum. Meas.*, vol. 71, pp. 1–10, 2022.

[9] A. Raza, R. Keshavarz, and N. Shariati, "In situ soil moisture monitoring using compact multiband sensing system for smart agriculture," *IEEE Trans. AgriFood Electron.*, vol. 3, no. 2, pp. 366–377, Sep. 2025.

[10] W. Wagner, G. Blöschl, P. Pampaloni, J.-C. Calvet, B. Bizzarri, J.-P. Wigneron, and Y. Kerr, "Operational readiness of microwave remote sensing of soil moisture for hydrologic applications," *Hydrol. Res.*, vol. 38, no. 1, pp. 1–20, Feb. 2007.

[11] D. Entekhabi et al., "The soil moisture active passive (SMAP) mission," *Proc. IEEE*, vol. 98, no. 5, pp. 704–716, May 2010.

[12] H.-J.-F. Benninga, R. van der Velde, and Z. Su, "Soil moisture content retrieval over meadows from Sentinel-1 and Sentinel-2 data using physically based scattering models," *Remote Sens. Environ.*, vol. 280, Oct. 2022, Art. no. 113191.

[13] S. Handbook, "Soil moisture active passive, mapping soil moisture and, freeze/thaw from space," National Aeronautics and Space Administration, Jet Propulsion Laboratory, California Institute of Technology, Tech. Rep., 2014. [Online]. Available: https://smap.jpl.nasa.gov/mission/description

[14] K. Liu, X. Li, S. Wang, and H. Zhang, "A robust gap-filling approach for European space agency climate change initiative (ESA CCI) soil moisture integrating satellite observations, model-driven knowledge, and spatiotemporal machine learning," *Hydrol. Earth Syst. Sci.*, vol. 27, no. 2, pp. 577–598, Jan. 2023.

[15] A. Gruber, W. A. Dorigo, W. Crow, and W. Wagner, "Triple collocation-based merging of satellite soil moisture retrievals," *IEEE Trans. Geosci. Remote Sens.*, vol. 55, no. 12, pp. 6780–6792, Dec. 2017.

[16] H. Ma, J. Zeng, X. Zhang, J. Peng, X. Li, P. Fu, M. H. Cosh, H. Letu, S. Wang, N. Chen, and J.-P. Wigneron, "Surface soil moisture from combined active and passive microwave observations: Integrating ASCAT and SMAP observations based on machine learning approaches," *Remote Sens. Environ.*, vol. 308, Jul. 2024, Art. no. 114197.

[17] J. Zhou, W. T. Crow, Z. Wu, J. Dong, H. He, and H. Feng, "A triple collocation-based 2D soil moisture merging methodology considering spatial and temporal non-stationary errors," *Remote Sens. Environ.*, vol. 263, Sep. 2021, Art. no. 112509.

[18] O. Sungmin and R. Orth, "Global soil moisture data derived through machine learning trained with in-situ measurements," *Sci. Data*, vol. 8, no. 1, p. 170, Jul. 2021.

[19] S. S. Yamaç, C. Şeker, and H. Negiş, "Evaluation of machine learning methods to predict soil moisture constants with different combinations of soil input data for calcareous soils in a semi arid area," *Agricult. Water Manage.*, vol. 234, May 2020, Art. no. 106121.

[20] A. Basak, K. M. Schmidt, and O. J. Mengshoel, "From data to interpretable models: Machine learning for soil moisture forecasting," *Int. J. Data Sci. Analytics*, vol. 15, no. 1, pp. 9–32, Jan. 2023.

[21] M. Saki, R. Keshavarz, D. Franklin, M. Abolhasan, J. Lipman, and N. Shariati, "Precision soil quality analysis using transformer-based data fusion strategies: A systematic review," 2024, *arXiv:2410.18353*.

[22] Y. Liu, C. Gong, L. Yang, and Y. Chen, "DSTP-RNN: A dual-stage two-phase attention-based recurrent neural network for long-term and multivariate time series prediction," *Expert Syst. Appl.*, vol. 143, Apr. 2020, Art. no. 113082.

[23] Y. Liu, Q. Zhang, L. Song, and Y. Chen, "Attention-based recurrent neural networks for accurate short-term and long-term dissolved oxygen prediction," *Comput. Electron. Agricult.*, vol. 165, Oct. 2019, Art. no. 104964.

[24] A. Vaswani, N. Shazeer, N. Parmar, J. Uszkoreit, L. Jones, A. N. Gomez, Ł. Kaiser, and I. Polosukhin, "Attention is all you need," in *Proc. Adv. Neural Inf. Process. Syst.*, vol. 30, 2017.

[25] Y. Wang and Y. Zha, "Comparison of transformer, LSTM and coupled algorithms for soil moisture prediction in shallow-groundwater-level areas with interpretability analysis," *Agricult. Water Manage.*, vol. 305, Dec. 2024, Art. no. 109120.

[26] A. Yinglan, G. Wang, P. Hu, X. Lai, B. Xue, and Q. Fang, "Root-zone soil moisture estimation based on remote sensing data and deep learning," *Environ. Res.*, vol. 212, Sep. 2022, Art. no. 113278.

[27] Y. Wang, L. Shi, Y. Hu, X. Hu, W. Song, and L. Wang, "A comprehensive study of deep learning for soil moisture prediction," *Hydrol. Earth Syst. Sci.*, vol. 28, no. 4, pp. 917–943, Feb. 2024.

[28] Z. Xiong, Z. Zhang, H. Gui, X. Chen, S. Hu, L. Gao, H. Yang, J. Qiu, and Q. Xin, "A meteorology-driven transformer network to predict soil moisture for agriculture drought forecasting," *IEEE Trans. Geosci. Remote Sens.*, vol. 63, 2025.

[29] L. Zhu, Q. Cai, J. Jin, S. Yuan, X. Shen, and J. P. Walker, "Multi-scale domain adaptation for high-resolution soil moisture retrieval from synthetic aperture radar in data-scarce regions," *J. Hydrol.*, vol. 657, Aug. 2025, Art. no. 133073.

[30] J.-S. Ay, R. Chakir, and J. L. Gallo, "Aggregated versus individual land-use models: Modeling spatial autocorrelation to increase predictive accuracy," *Environ. Model. Assessment*, vol. 22, no. 2, pp. 129–145, Apr. 2017.

[31] Z. Wu, S. Pan, F. Chen, G. Long, C. Zhang, and P. S. Yu, "A comprehensive survey on graph neural networks," *IEEE Trans. Neural Netw. Learn. Syst.*, vol. 32, no. 1, pp. 4–24, Jan. 2021.

[32] X. Zhang, C. Chen, Z. Meng, Z. Yang, H. Jiang, and X. Cui, "CoAtGIN: Marrying convolution and attention for graph-based molecule property prediction," in *Proc. IEEE Int. Conf. Bioinf. Biomed. (BIBM)*, Dec. 2022, pp. 374–379.

[33] G. Huo, Y. Zhang, B. Wang, J. Gao, Y. Hu, and B. Yin, "Hierarchical spatiotemporal graph convolutional networks and transformer network for traffic flow forecasting," *IEEE Trans. Intell. Transp. Syst.*, vol. 24, no. 4, pp. 3855–3867, Apr. 2023.

[34] J. Lu, Z. Yang, K. Huang, Z. Wang, Z. Zhou, and L. Zhou, "TGCA: A transformer GNN-based approach with cross-attention mechanism for steganographic text detection in social networks," in *Proc. IEEE Int. Conf. Acoust., Speech Signal Process. (ICASSP)*, Apr. 2025, pp. 1–5.

[35] S. Gheewala, S. Xu, S. Yeom, and S. Maqsood, "Exploiting deep transformer models in textual review based recommender systems," *Expert Syst. Appl.*, vol. 235, Jan. 2024, Art. no. 121120.

[36] A. Hawdon, D. McJannet, and J. Wallace, "Calibration and correction procedures for cosmic-ray neutron soil moisture probes located across Australia," *Water Resour. Res.*, vol. 50, no. 6, pp. 5029–5043, Jun. 2014.

[37] P. T. Setti and S. Tabibi, "Enhancing soil moisture estimates through the fusion of SMAP and GNSS-R data at 3-km resolution for daily mapping," *IEEE J. Sel. Topics Appl. Earth Observ. Remote Sens.*, vol. 18, pp. 5303–5316, 2025.

[38] M. Khaki, S.-C. Han, I.-Y. Yeo, and A. Frost, "The application of CYGNSS data for soil moisture and inundation mapping in Australia," *IEEE J. Sel. Topics Appl. Earth Observ. Remote Sens.*, vol. 14, pp. 10395–10404, 2021.

[39] W. Wang, C. Ma, X. Wang, J. Feng, L. Dong, J. Kang, R. Jin, and X. Li, "A soil moisture experiment for validating high-resolution satellite products and monitoring irrigation at agricultural field scale," *Agricult. Water Manage.*, vol. 304, Nov. 2024, Art. no. 109071.

[40] Y. Zheng, G. Coxon, R. Woods, D. Power, M. A. Rico-Ramirez, D. McJannet, R. Rosolem, J. Li, and P. Feng, "Evaluation of reanalysis soil moisture products using cosmic ray neutron sensor observations across the globe," *Hydrol. Earth Syst. Sci.*, vol. 28, no. 9, pp. 1999–2022, May 2024.

[41] N. Gorelick, M. Hancher, M. Dixon, S. Ilyushchenko, D. Thau, and R. Moore, "Google Earth engine: Planetary-scale geospatial analysis for everyone," *Remote Sens. Environ.*, vol. 202, pp. 18–27, Dec. 2017.

[42] T. Hengl, D. Consoli, X. Tian, T. W. Nauman, M. Nussbaum, M. S. Isik, L. Parente, Y.-F. Ho, R. Simoes, S. Gupta, A. Samuel-Rosa, T. Z. Horst, J. L. Safanelli, and N. Harris, "OpenLandMap-soildb: Global soil information at 30 m spatial resolution for 2000–2022+ based on spatiotemporal machine learning and harmonized legacy soil samples and observations," *Earth Syst. Sci. Data Discuss.*, vol. 2025, pp. 1–66, May 2025.

[43] M. J. Grundy, R. A. V. Rossel, R. D. Searle, P. L. Wilson, C. Chen, and L. J. Gregory, "Soil and landscape grid of Australia," *Soil Res.*, vol. 53, no. 8, pp. 835–844, Nov. 2015.

[44] I. Fuentes, J. Padarian, and R. W. Vervoort, "Towards near real-time national-scale soil water content monitoring using data fusion as a downscaling alternative," *J. Hydrol.*, vol. 609, Jun. 2022, Art. no. 127705.

[45] J. Yu, W. Zheng, L. Xu, F. Meng, J. Li, and L. Zhangzhong, "TPE-CatBoost: An adaptive model for soil moisture spatial estimation in the main maize-producing areas of China with multiple environment covariates," *J. Hydrol.*, vol. 613, Oct. 2022, Art. no. 128465.

[46] P. Oneill, S. Chan, E. Njoku, T. Jackson, R. Bindlish, J. Chaubell, and A. Colliander, "SMAP enhanced L3 radiometer global and polar grid daily 9 km ease-grid soil moisture, version 5," Tech. Rep., 2021.

[47] R. Reichle, G. De Lannoy, R. Koster, W. Crow, J. Kimball, Q. Liu, and M. Bechtold, "SMAP L4 global 3-hourly 9 km ease-grid surface and root zone soil moisture analysis update, version 7," Tech. Rep., 2022.

[48] B. Li et al., "Global GRACE data assimilation for groundwater and drought monitoring: Advances and challenges," *Water Resour. Res.*, vol. 55, no. 9, pp. 7564–7586, Sep. 2019.
[49] H. Hersbach et al., "The ERA5 global reanalysis," *Quart. J. Roy. Meteorological Soc.*, vol. 146, no. 730, pp. 1999–2049, 2020.
[50] J. Muñoz-Sabater, E. Dutra, A. Agustí-Panareda, C. Albergel, G. Arduini, G. Balsamo, S. Boussetta, M. Choulga, S. Harrigan, H. Hersbach, B. Martens, D. G. Miralles, M. Piles, N. J. Rodríguez-Fernández, E. Zsoter, C. Buontempo, and J.-N. Thépaut, "ERA5-land: A state-of-the-art global reanalysis dataset for land applications," *Earth Syst. Sci. Data*, vol. 13, no. 9, pp. 4349–4383, Sep. 2021.
[51] Y. Wang, R. Li, Q. Min, Y. Fu, Y. Wang, L. Zhong, and Y. Fu, "A three-source satellite algorithm for retrieving all-sky evapotranspiration rate using combined optical and microwave vegetation index at twenty AsiaFlux sites," *Remote Sens. Environ.*, vol. 235, Dec. 2019, Art. no. 111463.
[52] C. Song, G. Hu, Y. Wang, and X. Qu, "Downscaling ESA CCI soil moisture based on soil and vegetation component temperatures derived from MODIS data," *IEEE J. Sel. Topics Appl. Earth Observ. Remote Sens.*, vol. 15, pp. 2175–2184, 2022.
[53] O. G. Şahin and O. Gündüz, "A novel Land Surface Temperature reconstruction method and its application for downscaling surface soil moisture with machine learning," *J. Hydrol.*, vol. 634, May 2024, Art. no. 131051.
[54] N. Madhukumar, E. Wang, Y. Everingham, and W. Xiang, "Hybrid transformer network for soil moisture estimation in precision irrigation," *IEEE Access*, vol. 12, pp. 48898–48909, 2024.
[55] A. Sure and O. Dikshit, "Estimation of root zone soil moisture using passive microwave remote sensing: A case study for Rice and wheat crops for three states in the indo-gangetic basin," *J. Environ. Manage.*, vol. 234, pp. 75–89, Mar. 2019.
[56] Y. Shangguan, X. Min, and Z. Shi, "Inter-comparison and integration of different soil moisture downscaling methods over the Qinghai–Tibet Plateau," *J. Hydrol.*, vol. 617, Feb. 2023, Art. no. 129014.
[57] X. Bao, R. Zhang, X. He, A. Shama, G. Yin, J. Chen, H. Zhang, and G. Liu, "An integrated time-series relative soil moisture monitoring method based on a SAR backscattering model," *IEEE J. Sel. Topics Appl. Earth Observ. Remote Sens.*, vol. 18, pp. 1–22, 2025.
[58] S. Gu, Y. Zhou, L. Zhao, M. Ma, X. She, L. Zhang, and Y. Li, "A fast generative adversarial network combined with transformer for downscaling GRACE terrestrial water storage data in southwestern China," *IEEE Trans. Geosci. Remote Sens.*, vol. 62, 2024.
[59] E. Wig, R. Michaelides, and H. Zebker, "Fine-resolution measurement of soil moisture from cumulative InSAR closure phase," *IEEE Trans. Geosci. Remote Sens.*, vol. 62, 2024.
[60] P. Veličković, G. Cucurull, A. Casanova, A. Romero, P. Liò, and Y. Bengio, "Graph attention networks," 2017, *arXiv:1710.10903*.
[61] T. Chen, T. He, M. Benesty, V. Khotilovich, Y. Tang, H. Cho, K. Chen, R. Mitchell, I. Cano, and T. Zhou, "XGBoost: Extreme gradient boosting," R Package Version, Tech. Rep., 2015, pp. 1–4.
[62] S. Hochreiter, "The vanishing gradient problem during learning recurrent neural nets and problem solutions," *Int. J. Uncertainty, Fuzziness Knowl.-Based Syst.*, vol. 6, no. 2, pp. 107–116, Apr. 1998.
[63] T. Akiba, S. Sano, T. Yanase, T. Ohta, and M. Koyama, "Optuna: A next-generation hyperparameter optimization framework," in *Proc. 25th ACM SIGKDD Int. Conf. Knowl. Discovery Data Mining*, Jul. 2019, pp. 2623–2631.
[64] T. Blume, E. Zehe, and A. Bronstert, "Use of soil moisture dynamics and patterns at different spatio-temporal scales for the investigation of subsurface flow processes," *Hydrol. Earth Syst. Sci.*, vol. 13, no. 7, pp. 1215–1233, Jul. 2009.
[65] J. Gong, X. Jia, T. Zha, B. Wang, S. Kellomäki, and H. Peltola, "Modeling the effects of plant-interspace heterogeneity on water-energy balances in a semiarid ecosystem," *Agricult. Forest Meteorol.*, vol. 221, pp. 189–206, May 2016.
[66] Y. Wang, L. Gao, J. Li, and X. Peng, "Responses of deep soil moisture to direct rainfall and groundwater in the red soil critical zone: A four-stage pattern," *J. Hydrol.*, vol. 632, Mar. 2024, Art. no. 130864.
[67] A. Singh, K. Gaurav, G. K. Sonkar, and C.-C. Lee, "Strategies to measure soil moisture using traditional methods, automated sensors, remote sensing, and machine learning techniques: Review, bibliometric analysis, applications, research findings, and future directions," *IEEE Access*, vol. 11, pp. 13605–13635, 2023.
[68] Y. Wang, W. Wang, Z. Ma, M. Zhao, W. Li, X. Hou, J. Li, F. Ye, and W. Ma, "A deep learning approach based on physical constraints for predicting soil moisture in unsaturated zones," *Water Resour. Res.*, vol. 59, no. 11, p. 2023, Nov. 2023.
[69] L. Li, Y. Dai, Z. Wei, W. Shangguan, N. Wei, Y. Zhang, Q. Li, and X.-X. Li, "Enhancing deep learning soil moisture forecasting models by integrating physics-based models," *Adv. Atmos. Sci.*, vol. 41, no. 7, pp. 1326–1341, Jul. 2024.

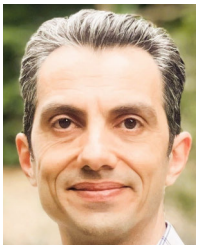

MAHDI SAKI received the Ph.D. degree from the School of Electrical and Data Engineering, University of Technology Sydney, in 2020. His doctoral research focused on big data classification in rail networks. Since completing his Ph.D. degree, he has made significant contributions to various data-driven industrial and research projects, developing several end-to-end AI/ML pipelines spanning diverse sectors, such as transportation, the IoT, telecom, and agriculture. He is currently working as an Applied Scientist with the School of Electrical and Data Engineering, University of Technology Sydney, where he applies AI/ML techniques in remote sensing-based data fusion in precision agriculture.



DANIEL FRANKLIN (Member, IEEE) received the Bachelor of Engineering degree (Hons.) in electrical engineering from the University of Wollongong, in 1999, and the Ph.D. degree in telecommunications engineering "enhancements to channel models, DMT modulation, and coding for channels subject to impulsive noise" from the University of Wollongong, in 2007. He is currently a Senior Lecturer with the School of Electrical and Data Engineering, University of Technology Sydney. His current research and commercial interests include split between radiation engineering, including positron emission tomography, computed tomography, radiotherapy, radiation dosimetry, pharmacokinetic modeling, and telecommunications engineering, including security applications and network protocols, multimedia, image and signal processing, wired and wireless communication systems, and communications protocols.



MEHRAN ABOLHASAN (Senior Member, IEEE) received the B.E. degree in computer engineering and the Ph.D. degree in telecommunications from the University of Wollongong, in 1999 and 2003, respectively. He has over 20 years of experience in research and development and serving in various research leadership roles. Some of these previous roles include working as the Director of research programs with the Faculty of Engineering and IT and the Deputy Head of school for research with the School of Electrical and Data Engineering, University of Technology Sydney, where he is currently the Leader of the Intelligent Networks and Applications Laboratory, Faculty of Engineering and IT. He has authored over 200 international publications and through his sustained track record of industry engagement, creation of new research ideas, and directions. He has successfully secured several research and development projects worth over eight million dollars. This includes external grants, such as ARC, CRC, industry, and government funded research projects. His current research interests include 5G/6G wireless networks, the Internet of Things, cybersecurity, software defined networking, intelligent transportation systems (ITS), urban greening, and digital agriculture.



JUSTIN LIPMAN (Senior Member, IEEE) builds innovation in connected technologies and thrives at the intersection of academia and industry. As both an industry focused Professor within the Telecom Research Unit (TRU) and the Director of the Cyber Digital Centre (CDC), University of Technology Sydney, he leverages over 20 years of industry expertise across various research and development leadership roles at Intel and Alcatel. Previously at UTS, he was the Director of the RF and Communications Technologies Laboratory and the Deputy Chief Scientist of the Food Agility Cooperative Research Centre. He has secured over $35M in industry focused research funding, driving innovation across networking, cybersecurity, RF, the IoT, digital agriculture, smart cities, and data privacy. He actively shapes future connected systems through research and standards development. As a dedicated bridge builder, he fuels impactful industry collaborations, translating research into real-world solutions and positioning himself at the forefront of innovation. He holds 24 U.S. patents and has published over 130 peer-reviewed articles.



NEGIN SHARIATI (Senior Member, IEEE) is currently an Associate Professor with the University of Technology Sydney, Australia. She established the state-of-the-art RF and Communication Technologies (RFCT) Research Laboratory, in 2018, where she is also the Founding Director, leading research and development in circuits and systems and wireless communication technologies. She led a three year research and development program, "Sensing Innovations Constellation," with the Food Agility Cooperative Research Centre (CRC), which focused on three key interrelated streams in digital agriculture: sensing, energy, and connectivity. This collaborative platform enabled multidisciplinary research and development with industry partners, addressing large-scale, and real-world challenges in agricultural technologies. She was the Director of Women in Engineering and IT with UTS, driving positive changes in equity and diversity in STEM. Since 2018, she has been holding a joint academic appointment at Hokkaido University, engaging in research and teaching activities in Japan. She has secured more than six million dollars in research funding across multiple ARC, CRC, industry, and government-funded research projects, where she has taken the lead chief investigator (CI) role and contributed as a CI team member. She leads a three year multidisciplinary research and development program "sustainable sensing, enhanced connectivity, and data analytics for precision urban and rural agriculture" in collaboration with NTT Group and Food Agility CRC.